Complex strain partitioning and heterogeneous extension rates during early rifting in the East Shetland Basin, northern North Sea

Johan S. Claringbould[1,2], Rebecca E. Bell[2], Christopher A-L. Jackson[2], Robert L. Gawthorpe[3], Tore Odinsen[4]

[1]Earthquake Research Institute, The University of Tokyo, 1-1-1 Yayoi, Bunkyo-ku, Tokyo, 113-0032, Japan
[2]Basins Research Group (BRG), Department of Earth Science and Engineering, Imperial College, London, SW7 2BP, UK
[3]Department of Earth Science, University of Bergen, Allégaten 41, 5007 Bergen, Norway
[4]Equinor ASA, Sandslihaugen 30, 5254 Sandsli, Norway

Corresponding author: Johan S. Claringbould (jsclaring@eri.u-tokyo.ac.jp)

Key points

- Regionally extensive subsurface data are used to quantify basin-wide strain behaviour during early stages of continental rifting
- Variable magnitude and rate of extension-related strain affect the structural development of upper-crustal fault systems and populations
- Three-dimensional strain behaviour during initial continental rift phases might be more complex than previously assumed

Abstract

The early stages of continental rifting are typified by growth of upper-crustal normal fault *systems* that are distributed relatively evenly across the width of the rift. Due to a lack of regional studies drawing on high-quality subsurface data, much less is known regarding the growth of fault *populations*, that is, an array of fault systems that collectively serve to accommodate rift-related stretching. Here we investigate the evolution of a pre-Triassic-to-Jurassic fault array in the East Shetland Basin, northern North Sea, using a regionally extensive subsurface dataset comprising multiple merged 3D seismic surveys (10,000 km^2), long (>75 km) 2D seismic profiles, and numerous boreholes. We use a number of techniques to quantify basin-wide strain behaviour over ~150 Myr. We show that pre-Triassic-to-Middle Triassic, rift-related strain was distributed across several sub-basins. Middle-to-Late Triassic extension rate decreased (14 m/Myr) and strain localized in the western part of the basin. The Early Jurassic locus of extensional strain initially shifted eastwards, before becoming widely distributed during the main, Middle-to-Late Jurassic rift phase, when extension rate (89 m/Myr) and factor (1.025) were at a maximum. We also demonstrate marked spatial variations in timing and magnitude of slip along-strike major fault systems. We argue that the East Shetland Basin evolved in response to an early phase of slow stretching, followed by local synrift cooling, and eventually rift narrowing during a phase defined by increasing extension rates. Our results imply that three-dimensional strain behaviour during the initial phases of continental rifting might be more complex than previously assumed.

Key words (6/6): East Shetland Basin, rift, strain behaviour, extension rate, fault

array, quantitative analyses

1. Introduction

Continental rifting is accommodated by the growth of upper-crustal normal fault *systems* and *populations*. Resolving the dynamics of continental rifting is important because normal faults control rift geomorphology and landscape development in time and space, and the erosion, transport and storage of sediment (Gawthorpe & Leeder, 2000). Normal faults are also seismogenic, meaning that, by understanding patterns of rift-related strain, we can more accurately assess the earthquake hazard in areas of continental rifting. Our current understanding of continental rift dynamics is largely based on studies focused on examples that have proceeded to full plate rupture and continental break-up (e.g., Gibbs, 1984; Brun, 1999; Ziegler & Cloetingh, 2004; Huismans & Beaumont, 2007; Nagel & Buck, 2007; Péron-Pinvidic et al., 2013), supplemented by those concentrating on failed rifts. The latter tend to focus on specific aspects or time periods of the rifting process, such as local and regional migration of extension-related strain (e.g., Behn et al., 2002; Cowie et al., 2005; Corti et al., 2013; Bell et al., 2014; Naliboff & Buiter, 2015), the influence of pre-existing structures on fault and rift geometry (e.g., Whipp et al., 2014; Duffy et al., 2015; Phillips et al., 2016; Henstra et al., 2019), and the effects of magmatism on rift development (e.g., Corti et al., 2003; Buck, 2006; Stab et al., 2015).

Extension and strain behaviour during lithospheric stretching (e.g., varying magnitude and rates) is also a specific aspect of rifting that has been studied extensively to constrain its relationship with the structural evolution of rift systems (e.g., England, 1983, Kuznir & Park, 1987; Bassi, 1995, Behn et al., 2002; Van Wijk & Cloetingh, 2002; Naliboff et al., 2017). Numerical and physical models of rift development, which simulate the formation and evolution of upper-crustal fault arrays, however, do not commonly consider how strain behaves in three dimensions. This often reflects the limited spatial and temporal resolution of such models, which allows them to only predict strain migration patterns in one or two dimensions (e.g., towards or away from the rift axis) (e.g., McClay, 1990; Cowie et al., 2000; Huismans et al., 2001; Behn et al., 2002; Ziegler & Cloetingh, 2004; Nagel & Buck, 2007; Naliboff et al., 2017). However, observations from individual faults or *fault systems* (i.e. a kinematically linked group of faults that are several km to 10's of km long) suggest that fault patterns and the overall accumulation of rift-related strain can be rather complex in three dimensions due to, for example, fault segment interaction, pre-existing structures, or rheologic heterogeneity in the upper-crust (e.g. Cowie et al., 2000; Walsh et al., 2003; Soliva et al., 2006; Putz-Perrier & Sanderson, 2008; Nixon et al., 2014; Whipp et al., 2014; Duffy et al., 2015; Jackson et al., 2017). Moreover, recent studies from young (<5 Myr old), still-active rifts (e.g., Gulf of Corinth Rift, Bell et al., 2009; Ford et al., 2013; Nixon et al., 2016), and now-inactive rifts that formed over considerably longer time periods (>150 Myr) (e.g., northern North Sea, Claringbould et al., 2017) suggest that, before rift narrowing occurs, the initial stretching phase involves the distribution of strain across a wide zone of stretched upper-crust. This results in the strongly diachronous growth of individual fault segments and systems that make up the larger, rift-related fault array during the early phases of continental rifting (e.g., Bell et al., 2009; Ford et al., 2013; Nixon et al., 2016; Claringbould et al., 2017). Péron-Pinvidic et al. (2013) argue that strain *migration* is in important aspect of continental rifting too. They propose that strain migrates during the transition from diffuse stretching and thinning of the upper-crust, to hyperextension and mantle exhumation, a progression that may also be linked to an increase in extension rate (e.g., Brune et al., 2016; Naliboff et al., 2017).

The role of strain rate on rift geometry and faulting patterns was first recognized by England (1983). England (1983) suggests that diffusion of heat during continental thinning will result in cooling of any level in the lithosphere as it is brought close to the surface. This will increase the total strength of the thinning lithosphere, as long as the lithospheric material have a temperature-dependent rheology (England, 1983). If the extension rate is relatively slow, this strengthening, which follows an initial weakening phase related to plate thinning, will prevent further extension (England, 1983). This so-called *synrift cooling* increases the creep stress in the thinned lithosphere once the temperature starts to drop, which causes the locus of maximum strain rate to move laterally and the rift to widen (Bassi, 1995). However, when the extension rate is relatively fast, synrift cooling will not occur, and necking and rift narrowing will take place (Kuznir & Park, 1987). This proposed relationship between extension rate and the resulting rift pattern has since been observed in and thus supported by numerous 2D, lithospheric-scale models (e.g., Bassi, 1995; Van Wijk & Cloetingh, 2002; Brune et al., 2016; Naliboff et al., 2017; Tetreault & Buiter, 2018). However, we have yet to use observations from natural rifts to constrain the timescale over which strain is distributed across a developing fault array during the early phases of continental rifting. Nor have we determined how changes in bulk extension magnitude and rate affect the temporal evolution of rift-wide strain.

Determining the geometry and growth of areally extensive (~10.000 km^2) normal fault populations, as opposed to individual fault systems, requires extensive, high-quality subsurface data. To this end, we focus on the East Shetland Basin, northern North Sea (Figure 1), and use a subsurface dataset comprising long (>75 km), deepimaging (~8 s TWT) regional 2D seismic reflection profiles, multiple, large, merged 3D seismic surveys (~10.000 km^2) that image to moderate depth (4.5-6.5 s TWT), and 107 hydrocarbon exploration wells. The northern North Sea represents a failed rift basin that developed over ~150 million years, which ceased before continental break up during the development of the North Viking Graben (Færseth, 1996). The East Shetland Basin, located on the western margin of the North Viking Graben, contains a large part of the fault array that accommodated continental extension (Figure 1). Our dataset allows a relatively high-resolution examination of: (i) long-term (~150 Myr), temporal and spatial changes in rift-related strain distribution and accumulation pattern across the entire basin, and (ii) local and regional variations in extension magnitude and rate through time. By resolving this, we aim to improve our understanding of how rift-related strain accumulates during the initial phases of continental rifting, and the effect of heterogeneous extension magnitudes and rates on the resulting rift geometry, thereby testing the predictions of physical and numerical models of continental extension.

2. Geological setting

The East Shetland Basin is located in the northern North Sea, offshore western Norway, on the western margin of the North Viking Graben (Figure 1). The present geometry of the basin is characterized by large (>25 km length), N- to NE-trending, east-dipping normal fault systems that bound 15-25 km wide half-grabens (Figures 1c and 2). Based on the interpretation of regional 2D seismic reflection lines, flexural backstripping, and tectono-stratigraphic forward modelling, previous work argues that the magnitude of extension varied between the Permian-Triassic and Late Jurassic rift phases (e.g., Roberts et al, 1993, 1995; Færseth, 1996). However, these studies were unable to resolve the detailed growth of individual fault systems or their host array. Subsequent to this, the increasing availability of 3D seismic reflection data permitted more detailed analysis of the geometry and growth of the individual fault systems in the East Shetland Basin, albeit most studies included only a relatively limited time interval (e.g., Late Jurassic) when set in the context of a rifting history that spanned ~150 Myr (e.g., Stratspey-Brent-Statfjord half graben, McLeod et al., 2000, 2002; Murchison-Statfjord North Fault, Young et al., 2001; Eastern East Shetland Basin, Cowie et al., 2005; Triassic Ninian and Alwyn North fields, Tomasso et al., 2008). Because they focus on relatively small areas and for only part of the somewhat protracted period of rifting, these studies only show how strain accumulates during the development of individual rift-related fault systems; how this is related to the longer-term dynamics of the larger host fault array remains unknown. In the eastern part of the East Shetland Basin, Cowie et al. (2005) document eastward strain migration towards the rift axis and overall rift narrowing during the Late Jurassic, suggesting this relates to the evolving thermal structure of the lithosphere. However, even the study of Cowie et al. (2005) covers only ~40% of the East Shetland Basin, over a limited time period (Middle-to-Late Jurassic). To test if their observation that strain migrates towards the centre of an ever-narrowing rift is valid across the entire western flank of the North Viking Graben, we need to study the entire East Shetland Basin over the ~150 Myr development of the northern North Sea rift.

In this study we develop the ideas of Claringbould et al. (2017), who show that, contrary to previous studies that argue for two discrete periods of rifting separated by a period of tectonic quiescence (e.g., Badley et al., 1988; Lee & Hwang, 1993; Roberts et al., 1993, 1995; Thomas & Coward, 1995; Færseth, 1996; Odinsen et al., 2000), rifting in the northern North Sea was protracted not punctuated. This is similar to Ravnås et al. (2000), who propose that the northern North Sea experienced Permian-to-Early Triassic and Middle-to-Late Jurassic rift episodes that were separated by an intervening Middle Triassic-to-Middle Jurassic *inter-rift* period (i.e. prolonged intervals with a duration of tens of Myr occurring between rift episodes, and characterized by more diffuse extension). However, due to limited resolution of their subsurface data set, Ravnås et al. (2000) are unable to neither clearly describe the style of rifting nor quantify the rate of rifting during this so-called inter-rift period and the previous Permian-to-Early Triassic rift episode. Furthermore, Claringbould et al. (2017) also argue that although pre-existing structures are able to influence subsequent rift-related structures, the larger lithosphere-scale thermal and rheologic heterogeneity may serve to dilute their control on rift geometry. Claringbould et al. (2017) qualitatively describe the evolution of the pre-Triassic-to-Late Jurassic fault array in a general sense, but do not quantify strain behaviour distributed through time and space (e.g., extension magnitude and rate, cf. Roberts et al. 1993, 1995). This study extends the somewhat qualitative study of Claringbould et al. (2017) to carefully quantify the ~150 Myr fault array evolution within the East Shetland Basin during eight time intervals that span 6 to 45 Myr.

3. Data and methods

3.1 Seismic reflection and well data

We use an extensive dataset comprising 2D and 3D time-migrated seismic reflection surveys that were collected between 2006 and 2012 (Figure 1b). More specifically, we use four, partly overlapping, 3D seismic "merged-surveys", which cover almost the whole East Shetland Basin (~10,000 km^2), image to depths of 4.5 to 6.5 s TWT (6 – 8 km), and that have a 12.5 × 12.5 m or 25 × 25 m in- and crossline spacing. We also use long (~50 km length) 2D seismic profiles that trend either NNE or WNW, which image to depths of ~8 s TWT (~10 km), and have a line spacing of ~5 km (Figure 1b). Seismic data quality ranges from excellent for some of the 3D surveys to moderate for some of the 2D profiles. In addition to the seismic reflection data, we use 107 hydrocarbon exploration wells to determine the age of the basin-fill, and hence the age of faulting and rate of rift-related strain accumulation. 82 of these wells are tied to the seismic data through the construction of synthetic seismograms (Figure 3).

3.2 Seismic interpretation and fault system analysis

We interpret nine key seismic horizons from pre-Triassic to the Base Cretaceous Unconformity (BCU) across an area of ~6800 km^2 (Figures 2 and 3). With the exception of the pre-Triassic horizons, all of these horizons are tied to the wells (Figures. 1b, 2 and 3). The three pre-Triassic horizons are picked based on their continuous, high-amplitude seismic character (Claringbould et al., 2017). Patruno and Reid (2017) identify Permian-Triassic to Devonian rift basins SW of our study area on the East Shetland Platform based on well data (Figure 1a), however, because it is difficult to directly constrain their ages in the East Shetland Basin, these horizons are named Pre-Triassic 1, 2, and 3.

We constrain the growth of major rift-related faults. “Major faults” are defined as those that are >3 km long, offset at least pre-Triassic deposits, and have >200 m of throw (Figure 1c). Such faults accommodate the majority of the rift-related strain (e.g., Fossen, 2010). Displacement data are based on horizon cut-off information collected on fault-normal seismic profiles that are spaced every ~625 m; this amounted to >14,000 values along 34 fault systems that have a combined length of 535 km (Figure 4). This spatial resolution of analysis is considered sufficient to analyse strain accumulation across the entire fault array during eight time periods that span 6 to 45 Myr over ~150 Myr. The horizon cut-off information is depth converted from ms TWT to depth (m) using the average time-depth relationship derived from 79 of our 107 wells (Figure 1c).

3.3 Fault array analysis

Expansion indices are used to constrain the temporal variation in fault-activity along the 34 fault systems and basin-wide extension magnitude (e.g., Thorsen, 1963; Cartwright et al, 1998; Bouroullec et al., 2004; Jackson & Rotevatn, 2013; Lewis et al., 2013; Reeve et al., 2015; Jackson et al., 2017) (Figure 4). The expansion index represents the *ratio* between the vertical (i.e. stratigraphic) thickness of time-equivalent hanging wall and footwall strata (see Supplemental material). Throw backstripping is used to determine the lateral distribution of strain across the fault array during specific time periods (e.g., Jackson et al., 2017) (see Supplemental material). Because backstripped throw essentially represents the vertical stratal thickness *difference* between the hanging wall and adjacent footwall, these values allow the expansion indices to put into perspective (see Supplemental material) (Figure 4). Furthermore, with the exception of the pre-Triassic units, we also calculate fault slip rates along the individual fault systems to constrain variation in strain across the fault array during Triassic-to-Late Jurassic rifting (see Supplemental material). The fault slip rate represents the backstripped displacement over time and is quoted in m/Myr. Because lithostratigraphic horizons do not necessarily represent chronostratigraphic surfaces (i.e. absolute time-lines), we use the average absolute ages of the lithostratigraphic boundaries from the wells across the East Shetland Basin to estimate horizon ages and thus fault slip rates (see Supplemental material).

In addition to the analyses of the 34 fault systems, we sum strain along three transect lines to investigate how basin-scale strain varied as rifting progressed (Figure 5). Three ~NW-trending transects are drawn approximately orthogonal to the analysed fault systems in the North, Centre, and South part of the basin (Figure 5). Where a transect line crosses one of the analysed fault systems, we calculate the horizontal extension at every location for each time period (see Supplemental material). These values are then summed per time period along each transect line (North, Centre, or South) and, additionally, by region (Western, Central or Eastern), to show how strain varied in time and space (Figure 5). Furthermore, the magnitude of extension (i.e. extension factor or β-factor) along the three transect lines is calculated for each time period, and with the exception of the pre-Triassic units for which the age is not constrained, extension rates are calculated along the three transects to again analyse how strain varies in space and time (see Supplemental material) (Figure 5). Similar to the fault slip rates, the average absolute ages of the lithostratigraphic boundaries from the wells across the East Shetland Basin are used to estimate the extension rates (see Supplemental material).

Lastly, we highlight how expansion index and backstripped throw values vary along the length of four of the largest, longest-lived faults (Eider, Ninian-Hutton, Cormorant, and Osprey faults; Figures 6-9), which are distributed across the fault array (Figure 10) (Claringbould et al. 2017). This allows us to illustrate how the development of these individual fault systems, which accommodated the bulk of the rift-related strain, relate to the strain accumulation at the basin-scale (Figures 4 and 5). We also undertake throw-depth (T-z) analyses at specific points along the length of these four major faults to assess how strain accumulated laterally along the fault over time (Figure 10) (e.g., Jackson et al., 2017).

4. Spatial and temporal strain variations in the East Shetland Basin

Temporal shifts in sediment depocentres across the East Shetland Basin reflect a complex growth of the rift-related fault array (Claringbould et al., 2017) (Figure 4). Here we quantify the development of major fault systems that make up the larger fault array, as well as calculating how rift-related strain varied through time at the basin scale (Figures 4 and 5).

4.1 Pre-Triassic-to-Middle Triassic (>245 Ma) (Units 1, 2, and the Teist Formation)

During the deposition of pre-Triassic Unit 1, 2, and the Lower-to-Middle Triassic Teist Formation several major faults in the Magnus, Tern, and Ninian sub-basins accumulated up to 1200 m of throw, corresponding to large expansion indices of 4 to 8 (Ninian West, Heather, and Cormorant faults, Figure 4a-c). During the deposition of pre-Triassic Units 1 and 2, summed extension values are highest in the eastern region (up to 2063 m), and along the south transect (up to 2696 m, with an extension factor of 1.042) (Figure 5b-c), while during the deposition of the overlying Lower-to-Middle Triassic Teist Formation the most extension occurred in the western region (1032 m) and along the centre transect (1369 m, with an extension factor of 1.059) (Figure 5b-c). During this >50 Myr time period, extensional strain was therefore rather distributed across the basin, forming several sub-basins.

4.2 Middle-to-Late Triassic (ca. 245-201 Ma) (Lunde and Lomvi formations)

Over the next ~40 Myr, during deposition of the Middle-to-Upper Triassic Lomvi and Lunde formations, overall strain accumulation decreased within the East Shetland Basin, with strain focusing towards the southwestern part of the fault array (Figure 4d). During this inter-rift period, an up to 800 m thick sediment depocentre developed next to the southern end of the west-dipping Eider Fault; only moderate activity (characterised by expansion indices up to 4) is observed on some of the larger structures east of this fault (Figure 4d). We calculate an average extension of 604 m for the Middle-to-Upper Triassic, which correlates to an average extension rate of 14 m/Myr (Figure 5b-d). Compared to the previous time interval this reflects a significant decrease extension rate (from 129 to 14 m/Myr) (Figure 5b).

4.3 Latest Triassic-to-Middle Jurassic (ca. 201-166 Ma) (Statfjord Formation, and Dunlin and Brent groups)

A significant shift in the locus of strain accumulation occurred during deposition of the uppermost Triassic-to-Lower Jurassic Statfjord Formation (Figure 4e). During this part of the inter-rift period, moderately thick (~50 and ~250 m), relatively tabular sedimentary depocentres developed in the hanging wall of major faults in the eastern half of the basin. These faults accumulated up to 300 m throw at this time, which was accompanied by expansion indices between 1.5 and 4 (Figure 4e). Most of this extension (385 m) accumulated in the Eastern region during this time interval (Figure

5b). Average extension rate during the latest Triassic-to-Early Jurassic had increased from 14 m/Myr (during the previous time period) to 23 m/Myr, with the highest extension rate (30 m/Myr) occurring in the north of the basin (i.e. along the northern transect; Figure 5d). This depositional pattern indicates that strain was no longer focused on a single fault in the western part of the basin (i.e. Eider Fault; Figure 4d), but was now widely distributed across the eastern part of the basin, being accommodated by slip on several major faults.

Moderate amounts of throw (up to 300 m, associated with expansion indices of up to 6) accumulated on these major faults in the east of the basin, indicating that strain continued to be focussed in this location for another ~20 Myr, during the subsequent deposition of the relatively thin (up to 300 m) Dunlin and Brent groups (Figure 4f and g). Most extension occurred in the Eastern region (599 m and 692 m) (Figure 5b). Average extension rate increased during the deposition of the Dunlin and Brent groups; 16 to 41 m/Myr, respectively (Figure 5d). The largest extension factor (up to 1.034) occurred in the centre of the basin (i.e. along the Centre transect line; Figure 5c)

4.4 Middle-to-Late Jurassic (ca. 166-145 Ma) (Viking Group)

In contrast to the preceding inter-rift period, when strain was relatively focused in the east of the East Shetland Basin, during subsequent deposition of the Middle-to-Upper Jurassic Viking Group, strain is now distributed across the whole basin (Figure 4h). Up to 1200 m of throw accumulated on the major faults, forming thick (up to 900 m) depocentres that were associated with high expansion indices (6 to 8) (Figure 4h). Extension was distributed relatively evenly across the different regions in the basin

(1849 m, 1908 m, and 1844 m) (Figure 5b). From the deposition of the Lower Jurassic Dunlin Group we observe an increase in strain accumulation and extension magnitude in the East Shetland Basin: expansion index from locally <4, to basin-wide 6 to 8 during the deposition of the Middle-to-Upper Jurassic Viking Group (Figure 4f-h). Both average extension factor (1.025 compared to 1.021) and extension rate (89 compared to 16 m/Myr) are significantly higher during the Middle-to-Late Jurassic than compared to the preceding, Early Jurassic rift phase (Figures 4f-h and 5c-d). Since the upper boundary of the Middle-to-Late Jurassic Viking Group is represented by a major regional unconformity (Base Cretaceous Unconformity) (Figures 2 and 3), the extension rate of this time interval is a minimum estimate, given as the observed sediment packages represents the minimum thickness.

5. Strain variations along strike of major fault systems

To investigate how basin-scale variations in strain (see section 4) relate to the growth of individual fault systems we undertake detailed kinematic analyses of four major fault system (Figures 6-9). These are four of the largest, longest-lived faults (Eider, Ninian-Hutton, Cormorant, and Osprey faults), which are distributed across the fault array. This includes an analysis of how slip rates varied during Triassic-to-Jurassic rifting (Figure 11).

During the deposition of pre-Triassic and earliest Triassic, strain was distributed across the basin, with most strain accommodated along the south transect line (see section 4.1). With the exception of the Osprey Fault (Figure 9a-c), which is located in the centre of the basin (Figure 10), the presence of multiple throw and expansion index maxima along the Eider, Ninian-Hutton, and Cormorant faults during the deposition of Unit 1 suggest these fault systems grew in response to growth and linkage of initially isolated segments (Figures 6a-c and 8a-c) (e.g., Jackson et al., 2017). Post-linkage, strain could have migrated along-strike, as illustrated by the Eider Fault, which saw an overall southwestwards migration of activity through time (Figure 6a-c).

During the Middle-to-Late Triassic inter-rift period, strain was primarily focussed in the Western region, along the Eider Fault (see section 4.2). At the southwestern tip of the Eider Fault, up to 900 m throw accumulated at this time, decreasing to ~200 m throw along strike towards the northeastern fault tip (Figure 6d). Relatively little strain was accommodated along the Cormorant and Osprey faults in the middle of the basin at this time (up to 500 m throw), with only small segments of these being active (Figure 8d and 9d), where the Ninian-Hutton Fault, located in the eastern part of the basin, being inactive (Figure 7d; see also T-z plots in Figure 10b-c and e). Furthermore, we observe an overall decrease in slip rate from the previous time interval (from up to 100 m/Myr to around 25 m/Myr) (Figure 11a-b), although, because the lower boundary of the Teist Formation is poorly constrained, these rates could be overestimated.

During the Middle Jurassic inter-rift period, strain accumulation shifted from the western to eastern part of the basin (see section 4.3). With exception of its northeastern tip, the Eider Fault was largely inactive, illustrated by the vertical intervals on the corresponding T-z plots (Figure 10d). Strain was distributed relatively evenly along the length of the Cormorant, Osprey, and Ninian-Hutton faults, during the deposition of the Statfjord Formation (Figures 7e and 9e), but the increase in expansion indices shows that more strain is accommodated around these faults over time (Figures 7f-g and 9f-g). Latest Triassic-to-Middle Jurassic slip rates increase from between 20-30 m/Myr during the deposition of the Statfjord Formation (Figure 11c) to 25-75 m/Myr during the deposition of the Brent Group (Figure 11d-e). Reactivation of the Ninian-Hutton Fault during deposition of the Statfjord Formation is clearly captured in the T-z plots (Figure 10e). For example, between Pre-Triassic 1 and 2, activity is observed along two segments (0 to ~30 km and ~45 to ~55 km), inactivity is marked by the vertical intervals up to the Top Lunde horizon along the entire length of the fault, after which the fault reactivates, marked by upwards decreasing throw (Figure 10e).

Lastly, during the Middle-to-Upper Jurassic deposition of the Viking Group, strain was distributed across the basin and accommodated by rapid slip (up to 100 m/Myr, Figure 11) on many of the major fault systems (see section 4.4). However, strain was not distributed evenly *along* the major fault systems, with clear throw maxima occurring despite the fact that fault segment linkage had occurred much earlier (i.e. pre-Triassic) (Figures 6-9).

6. Discussion

6.1. Temporal and spatial changes in the basin-scale distribution of rift-related strain

The northern North Sea has experienced a ~150 Myr rift history (Færseth, 1996). Despite rifting being rather protracted, the region experienced only the early phases of continental rifting (i.e. stretching and thinning phases, Péron-Pinvidic et al., 2013), and the basin was aborted before hyperextension, mantle exhumation, and magmatic oceanization occurred. Rift-related strain was partitioned in different parts of the basin and migrated through time (e.g., Færseth, 1996) (Figures 3-5 and 12). Spatial variations in the timing and magnitude of slip also occurred along-strike of major fault systems that make up the larger fault array, highlighting the heterogeneous nature of the early rift-related strain within the East Shetland Basin (Figures 6-12).

Strain migration along strike of individual fault systems is common, typically reflecting fault growth by segment linkage, rheological differences in the deforming host rock, and/or the presence of pre-existing structures (e.g., Cowie et al., 2000; McLeod et al., 2000, 2002; Young et al., 2001; Walsh et al., 2003; Soliva et al., 2006; Putz-Perrier & Sanderson, 2008; Tomasso et al., 2008; Nixon et al., 2014; Whipp et al., 2014; Duffy et al., 2015; Jackson et al., 2017). However, within the East Shetland Basin we see no clear evidence that these parameters dictated temporal variations in rift-related strain. Claringbould et al. (2017), propose that the evolution of the fault array geometry in the East Shetland Basin reflects narrowing of the thermal perturbation underlying the basin, suggesting that strain migration during the development of a population of upper-crustal normal fault systems is likely affected by lithospheric-scale parameters (e.g., Odinsen et al, 2000; Behn et al., 2002; Cowie et al., 2005; Nagel & Buck, 2007).

Complex strain migration patterns during the early phases of continental rifting could be caused by the emplacement of magmatic bodies (e.g., Corti et al., 2003; Buck, 2006; Stab et al., 2015). However, in the East Shetland Basin there is no clear evidence for significant rift-related magmatism, suggesting the emplacement of igneous bodies did not control the pattern of early rift-related strain accumulation. Other studies link rift-related strain migration to flexural downbending of the crust (e.g., Bayona & Thomas, 2003; Bell et al., 2014). Indeed, on the eastern margin of the northern North Sea, Bell et al. (2014) observe that the strain migrates away from the rift axis after a phase of Permian-Triassic rifting and Early Jurassic tectonic quiescence. However, flexural downbending of the upper-crust is typified by the overall migration of strain either towards or away from the principle rift axis, making it unlikely this is the cause for the far more complex faulting patterns observed in the East Shetland Basin. Cowie et al., (2005) show that Middle-to-Late Jurassic rift-related strain in the East Shetland Basin migrated towards the rift axis during the rift maximum, relating this to a change in the geometry of the underlying thermal perturbation associated with the initial phase of rift narrowing (i.e. an increase of vertical thermal gradient towards the rift axis; e.g., Huismans et al., 2001; Behn et al., 2002; Nagel & Buck, 2007). However, their study is focussed only on the eastern part of the East Shetland Basin and considered only Middle-to-Late Jurassic strain. By considering the entire basin and the full, ~150 Myr duration of rift activity, we show a much more complicated history comprising temporal and spatial changes in: (i) strain distribution (Figure 12), and (ii) extension magnitude and rate (Figures 4, 5d, and 11). Our study thus highlights that a full understanding of the early stages of continental breakup requires analysis of a sufficiently large study area, and needs to consider a sufficiently long period of rift development.

6.2. Variation in extension magnitude and rate during rifting

In the East Shetland Basin we observe that extension magnitudes and rates vary in space and time (Figures 4, 5, 11, 12). The changing bulk extension magnitude is expressed by temporal increases and decreases in average basin-wide expansion indices and extension factors (Figures 4 and 5c). Variations in extension rate are also highlighted by different extension and bulk fault slip rates between the studied time intervals (Figures 5d and 11). Our results suggest that extension and fault slip rates decrease and stay relatively low (≤30 m/Myr) for ~70 Myr during the Middle Triassic-to-Middle Jurassic inter-rift period, also reflected by relatively low average expansion indices (≤3) (Figures 4c-e, 5d, and 11a-c). From the Middle Jurassic, these rates increase again for ~30 Myr, with extension and fault slip rates of ≥50 m/Myr and average expansion indices of ≥5 during the Middle to Late Jurassic rift maximum (Figures 4 f-h5 and 11d-f).

We propose that changing extension rates may account for the patterns we observe, consistent with the predicted of lithospheric-scale numerical models (e.g., England, 1983; Houseman & England 1986; Kuznir & Park, 1987; Bassi, 1995; Van Wijk & Cloetingh, 2002; Péron-Pinvidic et al., 2013; Naliboff & Buiter., 2015; Brune et al., 2016; Naliboff et al., 2017). The distributed faulting that defined the pre-Triassic period may reflect the relatively slow, pre-Jurassic extension rates (Figure 12a-c) (e.g., Bassi, 1995; Naliboff et al., 2017). Subsequently, Triassic strain focussing on a small number of faults, while elsewhere in the basin minimal to no fault growth activity took place for ~45 Myr. We suggest that, during this inter-rift period, the relatively slow and decreasing extension rate induced local synrift cooling and was associated with limited fault activity (Figure 5d, 11c and 12d-e) (e.g., England, 1983; Kuznir & Park, 1987; Bassi, 1995; Van Wijk & Cloetingh, 2002; Naliboff & Buiter, 2015). Again, this interpretation is consistent with the predictions of previous 2D lithospheric-scale models (e.g., Van Wijk & Cloetingh, 2002; Naliboff et al., 2017). Van Wijk and Cloetingh (2002) observe a shift in the locus of maximum extension in their 2D lithosphere-scale numerical models when the lithosphere is initially extended at a relatively slow rate (<8000 m/Myr), allowing synrift cooling of the initially extended region. As a result, the "old" rifted sub-basin is abandoned, and extension concentrates in other areas of the larger rift system (Van Wijk & Cloetingh, 2002).

Van Wijk and Cloetingh (2002) compare their modelling results to several continental margins, including the Mid-Norwegian Margin, which is of comparable size and has a similar extension history to the East Shetland Basin. They find a close resemblance of the observed strain migration patterns and the results of their slow extension rate models (<8000 m/Myr); i.e. the time gap between successive rifting events, in which the locus of strain migrates, is of similar magnitude (~20-60 Myr) (Van Wijk & Cloetingh, 2002). Furthermore, our results show that Pre-Triassic faulting in the East Shetland Basin was characterized by distributed faulting, localized in several sub-basins (Figures 3, 4a-d). Naliboff et al. (2017) 2D lithosphere-scale numerical model to propose that a relatively slow (<5000 m/Myr) extension rate during the initial stage of rifting permits uniform lithospheric thinning accompanied by upper-crustal distributed faulting.

In contrast to initial slow and decreasing extension rates, we suggest that post-Triassic patterns of faulting in the East Shetland Basin are controlled by the increasing rate of lithospheric extension (Figure 5d) (e.g., England, 1983; Kuznir & Park, 1987; Bassi, 1995; Van Wijk & Cloetingh, 2002; Péron-Pinvidic et al., 2013; Brune et al., 2016; Naliboff et al., 2017). We propose that eastwards migration of strain during the latest-Triassic-to-Early Jurassic reflect the initial phase of rapid lithospheric necking and rift narrowing (e.g., Huismans et al., 2001; Behn et al., 2002; Cowie et al., 2005; Nagel & Buck, 2007; Péron-Pinvidic et al., 2013) (Figure 12e-g). The Middle-to-Late Jurassic rift maximum is characterized by the highest extension and fault slip rates (Figures 5d and 11f), and distributed faulting involving reactivation of some pre-Jurassic faults and the growth of new faults (Figures 5d and 11f and 12h). This is consistent with the results of Naliboff et al. (2017) who show that when extension rate increases (>5000 m/Myr), strain localises near a heated and weakened rift (i.e. rift narrowing) as the advective heating of the lithosphere exceeds the conductive cooling (Naliboff et al., 2017). Moreover, Naliboff et al. (2017) predict that when the extension rate increases after a period of relative slow extension (<5000 m/Myr), the upper-crustal rift pattern is characterized by a combination of new fault development and reactivation of the earlier developed, more widely distributed normal faults. Their numerical model prediction is thus consistent with our observations from the East Shetland Basin during the Middle-to-Late Jurassic rift maximum phase.

6.3 Comparing extension magnitudes and rates in relation to rift pattern evolution

The absolute transition velocity for which synrift cooling will or will not occur ranges from 1500 and 8000 m/Myr, depending on which numerical models is used (e.g., Bassi, 1995; Van Wijk & Cloetingh, 2002; Naliboff et al., 2017). This likely reflects variations in the initial conditions used by the different models, given that Bassi (1995) shows that this transition velocity is highly dependent on the rheology of the rifted lithosphere (see also Bassi, 1991 and Buck, 1991). It is therefore difficult to directly compare different models, models to natural examples, or natural rift systems.

There is a marked discrepancy between the extension rates we calculate in the East Shetland Basin (10-225 m/Myr), those used in numerical models (e.g., 5000-8000 m/Myr, Van Wijk & Cloetingh, 2002; Naliboff et al., 2017) and those determined in active rift systems by geodetic data (e.g., 4000 m/Myr, Main Ethiopian Rift, Bendick et al., 2006; 4500 m/Myr, Baikal Rift, Calais et al., 1998; 15000 m/Myr, Red Sea Rift, McClusky et al., 2010). This discrepancy likely reflects several factors that control the rate of plate stretching, as well as the resolving powers of the various analytical tools. First, we note that the extension rates quoted above are for the full rift width, whereas we only consider approximately a third of the width of the northern North Sea rift system. Most critically, our analysis does not include the main rift axis (i.e. the North Viking Graben) where most of the Middle-to-Late Jurassic extension took place (e.g., Færseth, 1996) (Figure 1a). Second, this variability may reflect the fact we are unable to calculate the true magnitude of upper crustal extension (and thus extension rate) using a relatively low spatial-resolution tool like seismic reflection data. For example, McDermott and Reston (2015) show that simply calculating fault heave (and thus extension magnitude) from seismic reflection data may lead to an underestimate of the true magnitude of upper-crustal extension, given that early formed, large-displacement faults may be rotated to such low angles that they are not imaged, and that such faults may be cross-cut by younger, lower-displacement structures (e.g., Pelican and Cormorant faults, and in the Tern and Ninian sub-basins, Figure 2b-c). Walsh and Watterson (1992) also note that the fractal distribution of fault sizes mean that up to 30% of extension can be taken up along sub-seismic faults (i.e. faults that are smaller than the seismic resolution). Such a discrepancy is further highlighted when one considers we calculate average extension factors of 1.024 and 1.034 for the Pre-Triassic-to-Triassic (Figure 5c), in contrast to the Permian (~1.25) and Triassic (~1.5) beta factor estimates for the entire rift derived from the tectono-stratigraphic forward models of Roberts et al. (1995) and Odinsen et al. (2000). For the Middle-to-Late Jurassic rift maximum we calculate an average extension factor of 1.025 (Figure 5c), which is somewhat lower than the value of ~1.15 estimated by Roberts et al. (1993) and (1995) for the East Shetland Basin.

6.4 Increasing extension rates during the initial development of natural rifts

We show that extension rate decreases during the Triassic and increases throughout the Jurassic in the East Shetland Basin (Figures 4, 5, and 11). We suggest that these changes are responsible for the observed patterns of rift-related faulting and overall rift geometry (Figures 5 and 12). Although difference in lithospheric characteristics between natural rift systems (e.g., rheology) complicate a direct comparison of extension rates (and its resultant effect on rift geometry; e.g., Bassi, 1995; Tetreault & Buiter, 2018), changes in relative extension rate during the rifting process have been observed at various rift systems (e.g., Corti et al., 2013; Ford et al., 2013; Brune et al., 2016). Based on numerical plate reconstructions, Brune et al. (2016), show that an abrupt acceleration in extension rate ~10 Myr before break up is apparent in the South Atlantic Rift, Central North Atlantic Rift, North America-Iberia Rift, Australia-Antarctica Rift, and South China Sea Opening. Brune et al. (2016), argue that this is the result of dynamic rift weakening: as long as the rift is strong, the extension rate is low, but with continued deformation the rift centre becomes successively weaker due to necking and strain softening. Loss of strength accelerates rifting, which results in continued strength loss and causes the conjugate rift segments to rapidly accelerate. Corti et al. (2013) also show that an increasing relative extension rate corresponds to the inward migration of active faulting towards the rift axis. However, their lithosphere-scale, centrifuge sand-box experiments show that inward migration of faults during rifting are also subject to other factors such as: thickness of brittle and ductile layers, width of the weak zone that localizes extension, and rift obliquity (Corti et al., 2013). During the development of the young (<5 Myr), still-active Corinth Rift, Ford et al. (2013) calculate a significant increase in extension rates based on extensive field data (600-1000 m/Myr, Late Pliocene; 2000-2500 m/Myr, Early Pleistocene; 3400-4800 m/Myr, Middle Pleistocene). Present-day geodetic extension rates across the Corinth Rift range from <5000 m/Myr in east and >10000-15000 m/Myr in west (Davies et al., 1997; Clarke et al., 1998; Briole et al., 2000; Avallone et al., 2005). Nixon et al. (2016), observe a significant rapid transition from a structurally complex, northward migrating rift to a predominantly asymmetric rift over a 300 kyr period, starting around the Middle Pleistocene. The Corinth rift (~100 × ~40 km) is of comparable size to the East Shetland Basin (~100 × ~100 km), and even though the latter only covers one part of the complete northern North Sea rift system, Nixon et al. (2016) also show a complex, asymmetric rift evolution during the initial stages of continental rifting. Following the predictions of Corti et al., (2013), Nixon et al. (2016) argue that rapid spatiotemporal variation in rift structure over a relatively short period of extension can reflect multiple parameters, including an increase in extension rate.

Our results suggest that changes in extension rate play an important role in the pattern of normal faulting we observe in the East Shetland Basin (and the northern North Sea in general) during pre-Triassic-to-Late Jurassic rifting. We propose that lack of a clear direction for strain migration, especially during pre-Jurassic extension, shows that the early stages of continental rifting is complex due to a range of underlying controlling factors (e.g. variation in extension rate, evolving geometry of underlying thermal perturbation, and the influence of faults developed during the initial stage of rifting). It is possible that the limited spatial and temporal dimensions used by the previous studies in the northern North Sea meant details of this heterogeneous strain distribution and complex rift pattern evolution were missed (e.g., Badley, et al., 1988; Lee & Hwang, 1993; Roberts et al., 1993, 1995; Thomas & Coward, 1995; Færseth, 1996; Odinsen et al., 2000; Cowie et al., 2005; Tomasso et al., 2008; Bell et al., 2014). Therefore, high-resolution observations and analyses across at least a full fault array, and over a considerable period of the rift event, are necessary to fully resolve the dynamics of continental rift development. Moreover, these details of three-dimensional strain behaviour during rift-related extension and its effect on the rift pattern evolution should be considered in future numerical and physical models.

7. Conclusion

Using an extensive, high-resolution subsurface dataset, we observe complex strain partitioning and varying extension rates during the ~150 Myr rift development of the East Shetland Basin. Comprehensive quantitative fault growth analyses across the entire width of the basin enable us to document the development of a fault array on one margin of a failed rift system and analyse the related strain distribution pattern over time (Figures 4-13). Our results highlight the complicated three-dimensional behaviour of strain in the upper-crust during the early stages of continental rifting.

For extended periods of time (>20 Myr) we find that strain is distributed across the full width of the basin where it accumulates and localizes at different parts, while in other parts minimal to no fault growth activity is observed. Furthermore, we calculate varying extension magnitudes and rates across the basin over time: average extension factor ranges between 1.020 and 1.034, and average extension rates range between 14 and 129 m/Myr. This variation marks different time intervals of relatively minimum and maximum rift activity during rifting in the East Shetland Basin. The heterogeneous strain distribution across the basin and varying extension rates are also shown in detail along-strike the individual fault systems that make up the larger fault array. Fault segment linkage and prior rift structures affect the localization of strain within these major faults, however it is unlikely that these dictate strain behaviour across the larger fault array. Instead our results suggest that changes in extension rate have significant control on strain distribution during the early stages of rifting. We argue that relatively lower and decreasing extension rates (14 m/Myr) lead to an inter-rift period that is characterized by distributed faulting and local synrift-cooling, while the relatively higher and increasing extension rates (from 16 m/Myr, Early Jurassic, to 89 m/Myr, Middle-to-Late Jurassic) lead to a heterogeneous strain distribution and, in the case of the East Shetland Basin, the gradual transition from lithospheric stretching to thinning and rift narrowing. Our results are consistent with the predictions of previous rift models that investigate the effect of relatively slow or fast extension rate on the rift pattern development.

Complex rift evolution during the initial phases of continental rifting and strain migration related to an increase of extension rate as observed in the East Shetland Basin are not uncommon among other natural rifts (e.g., Corinth Rift). However, this study illustrates the importance of the detailed analyses using high-resolution and regionally extensive 3D subsurface data over a considerable period of basin development, which results provide observations that can be compared with analogue rift models. Studies that propose a simple or multiphase rift evolution with a homogeneous strain distribution or directional strain migration pattern based on less extensive analyses across the full extent of the basin possibly overlook fault array development and local strain accumulations, especially during periods of relatively less rift activity. Heterogeneous three-dimensional strain behaviour during the initial phases of continental rifting as a result of varying extension rate and magnitude are not typically generated in simple rift models, yet can be a significant aspect of rift dynamics.

Acknowledgements

We acknowledge funding from the Equinor Departmental Scholarship at Imperial College London and the MultiRift Project, which is funded by the Research Council of Norway (PETROMAKS Project number 215591/E30) and Equinor (data provider/supporter) to the University of Bergen, and partners Imperial College London, University of Manchester, and University of Oslo. We thank Al Fraser and Jon Bull for their comments on the initial version of this work. For their involvement in providing the data and permission to publish, we are grateful Thomas Weight, Tom Dreyer, Mark Lawson, Claire Thomas, and Bart Hendriks at Equinor, Richard Lamb and Emma Taylor at PGS, and Bent Kjølhamar at TGS. Schlumberger is thanked for providing Petrel to Imperial College London and the Earthquake Research Institute of The University of Tokyo. We also thank the members of the Basins Research Group at Imperial College London and the MultiRift Project, in particular Thilo Wrona, for fruitful discussions.

The data used for this study are publically available for download via the UK National Data Repository (NDR) (https://ndr.ogauthority.co.uk) for the United Kingdom side, and the DISKOS online portal (Diskos) (https://portal.diskos.cgg.com) for the Norwegian side.

References

Avallone, A., Briole, P., Agatza-Balodimou, A. M., Billiris, H., Charade, O., Mitsakaki, C., ... & Veis, G. (2004). Analysis of eleven years of deformation measured by GPS in the Corinth Rift Laboratory area. *Comptes Rendus Geoscience*, *336*(4-5), 301–311. https://doi.org/10.1016/j.crte.2003.12.007

Badley, M. E., Price, J. D., Dahl, C. R., & Agdestein, T. (1988). The structural evolution of the northern Viking Graben and its bearing upon extensional modes of basin formation. *Journal of the Geological Society*, *145*(3), 455–472. https://doi.org/10.1144/gsjgs.145.3.0455

Bassi, G. (1991). Factors controlling the style of continental rifting: insights from numerical modelling. *Earth and Planetary Science Letters*, *105*(4), 430–452. https://doi.org/10.1016/0012-821X(91)90183-I

Bassi, G. (1995). Relative importance of strain rate and rheology for the mode of continental extension. *Geophysical Journal International*, *122*(1), 195–210. https://doi.org/10.1111/j.1365-246X.1995.tb03547.x

Behn, M. D., Lin, J., & Zuber, M. T. (2002). A continuum mechanics model for normal faulting using a strain-rate softening rheology: Implications for thermal and rheological controls on continental and oceanic rifting. *Earth and Planetary Science Letters*, *202*(3-4), 725–740. https://doi.org/10.1016/S0012-821X(02)00792-6

Bell, R. E., Jackson, C. A-L., Whipp, P. S., & Clements, B. (2014). Strain migration during multiphase extension: Observations from the northern North Sea. *Tectonics*, *33*(10), 1936–1963. https://doi.org/10.1002/2014TC003551

Bell, R. E., McNeill, L. C., Bull, J. M., Henstock, T. J., Collier, R. L., & Leeder, M. R. (2009). Fault architecture, basin structure and evolution of the Gulf of Corinth Rift, central Greece. *Basin Research*, *21*(6), 824–855. https://doi.org/10.1111/j.1365-2117.2009.00401.x

Bouroullec, R., Cartwright, J. A., Johnson, H. D., Lansigu, C., Quémener, J. M., & Savanier, D. (2004). Syndepositional faulting in the Grès d'Annot Formation, SE France: High-resolution kinematic analysis and stratigraphic response to growth faulting. *Geological Society, London, Special Publications*, *221*(1), 241–265. https://doi.org/10.1144/GSL.SP.2004.221.01.13

Bayona, G., & Thomas, W. A. (2003). Distinguishing fault reactivation from flexural deformation in the distal stratigraphy of the peripheral Blountian foreland basin, southern Appalachians, USA. *Basin Research*, *15*(4), 503–526. https://doi.org/10.1046/j.1365-2117.2003.00217.x

Bendick, R., McClusky, S., Bilham, R., Asfaw, L., & Klemperer, S. (2006). Distributed Nubia—Somalia relative motion and dike intrusion in the Main Ethiopian Rift. *Geophysical Journal International*, *165*(1), 303–310. https://doi.org/10.1111/j.1365-246X.2006.02904.x

Briole, P., Rigo, A., Lyon-Caen, H., Ruegg, J. C., Papazissi, K., Mitsakaki, C., Balodimou, A., Veis, G., Hatzfeld D., & Deschamps, A. (2000). Active deformation of the Corinth rift, Greece: results from repeated Global Positioning System surveys between 1990 and 1995. *Journal of Geophysical Research: Solid Earth*, *105*(B11), 25605–25625. https://doi.org/10.1029/2000JB900148

Brun, J-P. (1999). Narrow rifts versus wide rifts: inferences for the mechanics of rifting from laboratory experiments. *Philosophical Transactions of the Royal Society of London. Series A: Mathematical, Physical and Engineering Sciences*, *357*(1753), 695–712. https://doi.org/10.1098/rsta.1999.0349

Brune, S., Williams, S. E., Butterworth, N. P., & Müller, R. D. (2016). Abrupt plate accelerations shape rifted continental margins. *Nature*, *536*(7615), 201–204. https://doi.org/10.1038/nature18319

Buck, W. R. (1991). Modes of continental lithospheric extension. *Journal of Geophysical Research: Solid Earth*, *96*(B12), 20161–20178. https://doi.org/10.1029/91JB01485

Buck, W. R. (2006). The role of magma in the development of the Afro-Arabian Rift System. *Geological Society, London, Special Publications*, *259*(1), 43–54. https://doi.org/10.1144/GSL.SP.2006.259.01.05

Calais, E., Lesne, O., Déverchère, J., San'kov, V., Lukhnev, A., Miroshnitchenko, A., Buddo, V., Levi, K., Zalutzky, V., & Bashkuev, Y. (1998). Crustal deformation in the Baikal rift from GPS measurements. *Geophysical Research Letters*, *25*(21), 4003–4006. https://doi.org/10.1029/1998GL900067

Cartwright, J., Bouroullec, R., James, D., & Johnson, H. (1998). Polycyclic motion history of some Gulf Coast growth faults from high-resolution displacement analysis. *Geology*, *26*(9), 819–822. https://doi.org/10.1130/0091-7613(1998)026<0819:PMHOSG>2.3.CO;2

Clarke, P. J., Davies, R. R., England, P. C., Parsons, B., Billiris, H., Paradissis, D., ... & Bingley, R. (1998). Crustal strain in central Greece from repeated GPS measurements in the interval 1989–1997. *Geophysical Journal International*, *135*(1), 195–214. https://doi.org/10.1046/j.1365-246X.1998.00633.x

Claringbould, J. S., Bell, R. E., Jackson, C. A-L., Gawthorpe, R. L., & Odinsen, T. (2017). Pre-existing normal faults have limited control on the rift geometry of the northern North Sea. *Earth and Planetary Science Letters*, *475*, 190–206. https://doi.org/10.1016/j.epsl.2017.07.014

Corti, G., Bonini, M., Conticelli, S., Innocenti, F., Manetti, P., & Sokoutis, D. (2003). Analogue modelling of continental extension: a review focused on the relations between the patterns of deformation and the presence of magma. *Earth-Science Reviews*, *63*(3-4), 169–247. https://doi.org/10.1016/S0012-8252(03)00035-7

Corti, G., Ranalli, G., Agostini, A., & Sokoutis, D. (2013). Inward migration of faulting during continental rifting: Effects of pre-existing lithospheric structure and extension rate. *Tectonophysics*, *594*, 137–148. https://doi.org/10.1016/j.tecto.2013.03.028

Cowie, P. A., Gupta, S., & Dawers, N. H. (2000). Implications of fault array evolution for synrift depocentre development: insights from a numerical fault growth model. *Basin Research*, *12*(3-4), 241–261. https://doi.org/10.1029/2017TC004776

Cowie, P. A., Underhill, J. R., Behn, M. D., Lin, J., & Gill, C. E. (2005). Spatio-temporal evolution of strain accumulation derived from multi-scale observations of Late Jurassic rifting in the northern North Sea: A critical test of models for lithospheric extension. *Earth and Planetary Science Letters*, *234*(3-4), 401–419. http://doi.org/ 10.1016/j.epsl.2005.01.039

Davies, R., England, P. C., Parsons, B., Billiris, H., Paradissis, D., & Veis, G. (1997). Geodetic strain of Greece in the interval 1892–1992. *Journal of Geophysical Research: Solid Earth*, *102*(B11), 24571–24588. https://doi.org/10.1029/97JB01644

Duffy, O. B., Bell, R. E., Jackson, C. A-L., Gawthorpe, R. L., & Whipp, P. S. (2015). Fault growth and interactions in a multiphase rift fault network: Horda Platform, Norwegian North Sea. *Journal of Structural Geology*, *80*, 99–119. https://doi.org/10.1016/j.jsg.2015.08.015

England, P. (1983). Constraints on extension of continental lithosphere. *Journal of Geophysical Research: Solid Earth*, *88*(B2), 1145–1152. https://doi.org/10.1029/JB088iB02p01145

Færseth, R. B. (1996). Interaction of Permo-Triassic and Jurassic extensional fault-blocks during the development of the northern North Sea. *Journal of the Geological Society*, *153*(6), 931–944. https://doi.org/10.1144/gsjgs.153.6.0931

Ford, M., Rohais, S., Williams, E. A., Bourlange, S., Jousselin, D., Backert, N., & Malartre, F. (2013). Tectono-sedimentary evolution of the western Corinth rift (Central Greece). *Basin Research*, *25*(1), 3–25. https://doi.org/10.1111/j.1365-2117.2012.00550.x

Fossen, H. (2010), *Structural Geology*, Cambridge, UK: Cambridge University Press

Gawthorpe, R. L., & Leeder, M. R. (2000). Tectono-sedimentary evolution of active extensional basins. *Basin Research*, *12*(3-4), 195–218. https://doi.org/10.1111/j.1365-2117.2000.00121.x

Gibbs, A. D. (1984). Structural evolution of extensional basin margins. *Journal of the Geological Society*, *141*(4), 609–620. https://doi.org/10.1144/gsjgs.141.4.0609

Henstra, G. A., Berg Kristensen, T., Rotevatn. A., & Gawthorpe, R. L. (2019). How do pre-existing normal faults influence rift geometry? A comparison of adjacent basins with contrasting underlying structure on the Lofoten Margin, Norway. *Basin Research*, 2019;00, 1–15. https://doi.org/10.1111/bre.12358

Houseman, G., & England, P. (1986). A dynamical model of lithosphere extension and sedimentary basin formation. *Journal of Geophysical Research: Solid Earth*, *91*(B1), 719–729. https://doi.org/10.1029/JB091iB01p00719

Huismans, R. S., Podladchikov, Y. Y., & Cloetingh, S. A. P. L. (2001). Transition from passive to active rifting: Relative importance of asthenospheric doming and passive extension of the lithosphere. *Journal of Geophysical Research: Solid Earth*, *106*(B6), 11271–11291. https://doi.org/10.1029/2000JB900424

Huismans, R. S., & Beaumont, C. (2007). Roles of lithospheric strain softening and heterogeneity in determining the geometry of rifts and continental margins. *Geological Society, London, Special Publications*, *282*(1), 111–138. https://doi.org/10.1144/SP282.6

Jackson, C. A-L., Bell, R. E., Rotevatn, A., & Tvedt, A. B. (2017). Techniques to determine the kinematics of synsedimentary normal faults and implications for fault growth models. *Geological Society, London, Special Publications*, *439*(1), 187–217. https://doi.org/10.1144/SP439.22

Jackson, C. A-L., & Rotevatn, A. (2013). 3D seismic analysis of the structure and evolution of a salt-influenced normal fault zone: a test of competing fault growth models. *Journal of Structural Geology*, *54*, 215–234. https://doi.org/10.1016/j.jsg.2013.06.012

Kusznir, N. J., & Park, R. G. (1987). The extensional strength of the continental lithosphere: its dependence on geothermal gradient, and crustal composition and thickness. *Geological Society, London, Special Publications*, *28*(1), 35–52. https://doi.org/10.1144/GSL.SP.1987.028.01.04

Lee, M. J., & Hwang, Y. J., (1993). Tectonic evolution and structural styles of the East Shetland Basin. *Geological Society, London, Petroleum Geology Conference Series*, *4*, 1137–1149. https://doi.org/10.1144/0041137

Lewis, M. M., Jackson, C. A-L., & Gawthorpe, R. L. (2013). Salt-influenced normal fault growth and forced folding: The Stavanger Fault System, North Sea. *Journal of Structural Geology*, *54*, 156-173. https://doi.org/10.1016/j.jsg.2013.07.015

McClay, K. R. (1990). Extensional fault systems in sedimentary basins: a review of analogue model studies. *Marine and petroleum Geology*, *7*(3), 206–233. https://doi.org/10.1016/0264-8172(90)90001-W

McClusky, S., Reilinger, R., Ogubazghi, G., Amleson, A., Healeb, B., Vernant, P., Sholan, J., Fisseha, S., Asfaw, L., Bendick, & R., Kogan, L. (2010). Kinematics of the southern Red Sea–Afar Triple Junction and implications for plate dynamics. *Geophysical Research Letters*, *37*(5), L05301. https://doi.org/10.1029/2009GL041127

McDermott, K., & Reston, T. (2015). To see, or not to see? Rifted margin extension. *Geology*, *43*(11), 967–970. https://doi.org/10.1130/G36982.1

McLeod, A. E., Dawers, N. H., & Underhill, J. R. (2000). The propagation and linkage of normal faults: insights from the Strathspey–Brent–Statfjord fault array, northern North Sea. *Basin Research*, *12*(3-4), 263–284. https://doi.org/10.1111/j.1365-2117.2000.00124.x

McLeod, A. E., Underhill, J. R., Davies, S. J., & Dawers, N. H. (2002). The influence of fault array evolution on synrift sedimentation patterns: Controls on deposition in the Strathspey-Brent-Statfjord half graben, northern North Sea. *AAPG Bulletin*, *86*(6), 1061–1093. https://doi.org/10.1306/61EEDC24-173E-11D7-8645000102C1865D

Nagel, T. J., & Buck, W. R. (2007). Control of rheological stratification on rifting geometry: a symmetric model resolving the upper plate paradox. *International Journal of Earth Sciences*, *96*(6), 1047–1057. https://doi.org/10.1007/s00531-007-0195-x

Naliboff, J. B., & Buiter, S. J. H. (2015). Rift reactivation and migration during multiphase extension. *Earth and Planetary Science Letters*, *421*, 58–67. https://doi.org/10.1016/j.epsl.2015. 03.050

Naliboff, J. B., Buiter, S. J. H., Péron-Pinvidic, G., Osmundsen, P. T., & Tetrault, J. L. (2017). Complex fault interaction controls continental rifting. *Nature Communications*, *8*(1), 1179. https://doi.org/10.1038/s41467-017-00904-x

Nixon, C. W., Bull, J. M., & Sanderson, D. J. (2014). Localized vs distributed deformation associated with the linkage history of an active normal fault, Whakatane Graben, New Zealand. *Journal of Structural Geology*, *69*, 266-280. https://doi.org/10.1016/j.jsg.2014.06.005

Nixon, C. W., McNeill, L. C., Bull, J. M., Bell, R. E., Gawthorpe, R. L., Henstock, T. J., ... & Ferentinos, G. (2016). Rapid spatiotemporal variations in rift structure during development of the Corinth Rift, central Greece. *Tectonics*, *35*(5), 1225–1248. https://doi.org/10.1002/2015TC004026

Odinsen, T., Reemst, P., Van der Beek, P., Faleide, J. I., & Gabrielsen, R. H. (2000). Permo-Triassic and Jurassic extension in the northern North Sea: results from tectonostratigraphic forward modelling. *Geological Society, London, Special Publications*, *167*(1), 83–103. https://doi.org/10.1144/GSL.SP.2000.167.01.05

Patruno, S., & Reid, W. (2017). New plays on the Greater East Shetland Platform (UKCS Quadrants 3, 8–9, 14–16)–part 2: Newly reported Permo-Triassic intra-platform basins and their influence on the Devonian-Paleogene prospectivity of the area. *First Break*, *35*(1), 59–69.

Péron-Pinvidic, G., Manatschal, G., & Osmundsen, P. T. (2013). Structural comparison of archetypal Atlantic rifted margins: A review of observations and concepts. *Marine and Petroleum Geology*, *43*, 21–47. https://doi.org/10.1016/j.marpetgeo.2013.02.002

Phillips, T. B., Jackson, C. A-L, Bell, R. E., Duffy, O. B., & Fossen, H. (2016). Reactivation of intrabasement structures during rifting: A case study from offshore southern Norway. *Journal of Structural Geology*, *91*, 54–-73. https://doi.org/10.1016/j.jsg.2016.08.008

Putz-Perrier, M. W., & Sanderson, D. J. (2008). The distribution of faults and fractures and their importance in accommodating extensional strain at Kimmeridge Bay, Dorset, UK. *Geological Society, London, Special Publications*, *299*(1), 97–111. https://doi.org/10.1144/SP299.6

Ravnås, R., Nøttvedt, A., Steel, R. J., & Windelstad, J. (2000). Syn-rift sedimentary architectures in the Northern North Sea. *Geological Society, London, Special Publications*, *167*(1), 133–177. https://doi.org/10.1144/GSL.SP.2000.167.01.07

Reeve, M. T., Bell, R. E., & Jackson, C. A-L. (2014). Origin and significance of intra-basement seismic reflections offshore western Norway. *Journal of the Geological Society*, *171*(1), 1–4. https://doi.org/10.1144/jgs2013-020

Roberts, A. M., Yielding, G., Kusznir, N. J., Walker, I. M., & Dorn-Lopez, D. (1993). Mesozoic extension in the North Sea: constraints from flexural backstripping, forward modelling and fault populations. Geological *Society, London, Petroleum Geology Conference Series*, *4*, 1123–1136. https://doi.org/10.1144/0041123

Roberts, A. M., Yielding, G., Kusznir, N. J., Walker, I. M., & Dorn-Lopez, D. (1995). Quantitative analysis of Triassic extension in the northern Viking Graben. *Journal of the Geological Society*, *152*(1), 15–26. https://doi.org/10.1144/gsjgs.152.1.0015

Stab, M., Bellahsen, N., Pik, R., Quidelleur, X., Ayalew, D., & Leroy, S. (2016). Modes of rifting in magma-rich settings: Tectono-magmatic evolution of Central Afar. *Tectonics*, *35*(1), 2–38. https://doi.org/10.1002/ 2015TC003893

Soliva, R., Benedicto, A., & Maerten, L. (2006). Spacing and linkage of confined normal faults: importance of mechanical thickness. *Journal of Geophysical Research: Solid Earth*, *111*(B1), B01402. https://doi.org/10.1029/2004JB003507

Tetreault, J. L., & Buiter, S. J. H. (2018). The influence of extension rate and crustal rheology on the evolution of passive margins from rifting to break-up. *Tectonophysics*, *746*, 155–172. https://doi.org/10.1016/j.tecto.2017.08.029

Thomas, D. W., & Coward, M. P. (1995). Late Jurassic–Early Cretaceous inversion of the northern East Shetland Basin, northern North Sea. *Geological Society, London, Special Publications*, *88*, 275–306. https://doi.org/10.1144/GSL.SP.1995.088.01.16

Thorsen, C.E. (1963). Age of growth faulting in the southeast Louisiana. *Transactions of the Gulf Coast Association of Geological Societies*, *13*, 103–110.

Tomasso, M., Underhill, J. R., Hodgkinson, R. A., & Young, M. J. (2008). Structural styles and depositional architecture in the Triassic of the Ninian and Alwyn North fields: Implications for basin development and prospectivity in the Northern North Sea. *Marine and Petroleum Geology*, *25*(7), 588–605. https://doi.org/10.1016/j.marpetgeo.2007.11.007

Walsh, J. J., Bailey, W. R., Childs, C., Nicol, A., & Bonson, C. G. (2003). Formation of segmented normal faults: a 3-D perspective. *Journal of Structural Geology*, *25*(8), 1251–1262. https://doi.org/10.1016/S0191-8141(02)00161-X

Walsh, J. J., & Watterson, J. (1992). Populations of faults and fault displacements and their effects on estimates of fault-related regional extension. *Journal of Structural Geology*, *14*(6), 701–712. https://doi.org/10.1016/0191-8141(92)90127-I

Whipp, P. S., Jackson, C. A-L., Gawthorpe, R. L., Dreyer, T., & Quinn, D. (2014). Normal fault array evolution above a reactivated rift fabric; a subsurface example from the northern Horda Platform, Norwegian North Sea. *Basin Research*, *26*(4), 523–549. https://doi.org/10.1111/bre.12050

van Wijk, J. W., & Cloetingh, S. A. P. L. (2002). Basin migration caused by slow lithospheric extension. *Earth and Planetary Science Letters*, *198*(3-4), 275–288. https://doi.org/10.1016/S0012-821X(02)00560-5

Young, M. J., Gawthorpe, R. L., & Hardy, S. (2001). Growth and linkage of a segmented normal fault zone; the Late Jurassic Murchison–Statfjord North Fault, northern North Sea. *Journal of Structural Geology*, *23*(12), 1933–1952. https://doi.org/10.1016/S0191-8141(01)00038-4

Ziegler, P. A., & Cloetingh, S. (2004). Dynamic processes controlling evolution of rifted basins. *Earth-Science Reviews*, *64*(1-2), 1–50. https://doi.org/10.1016/S0012-8252(03)00041-2

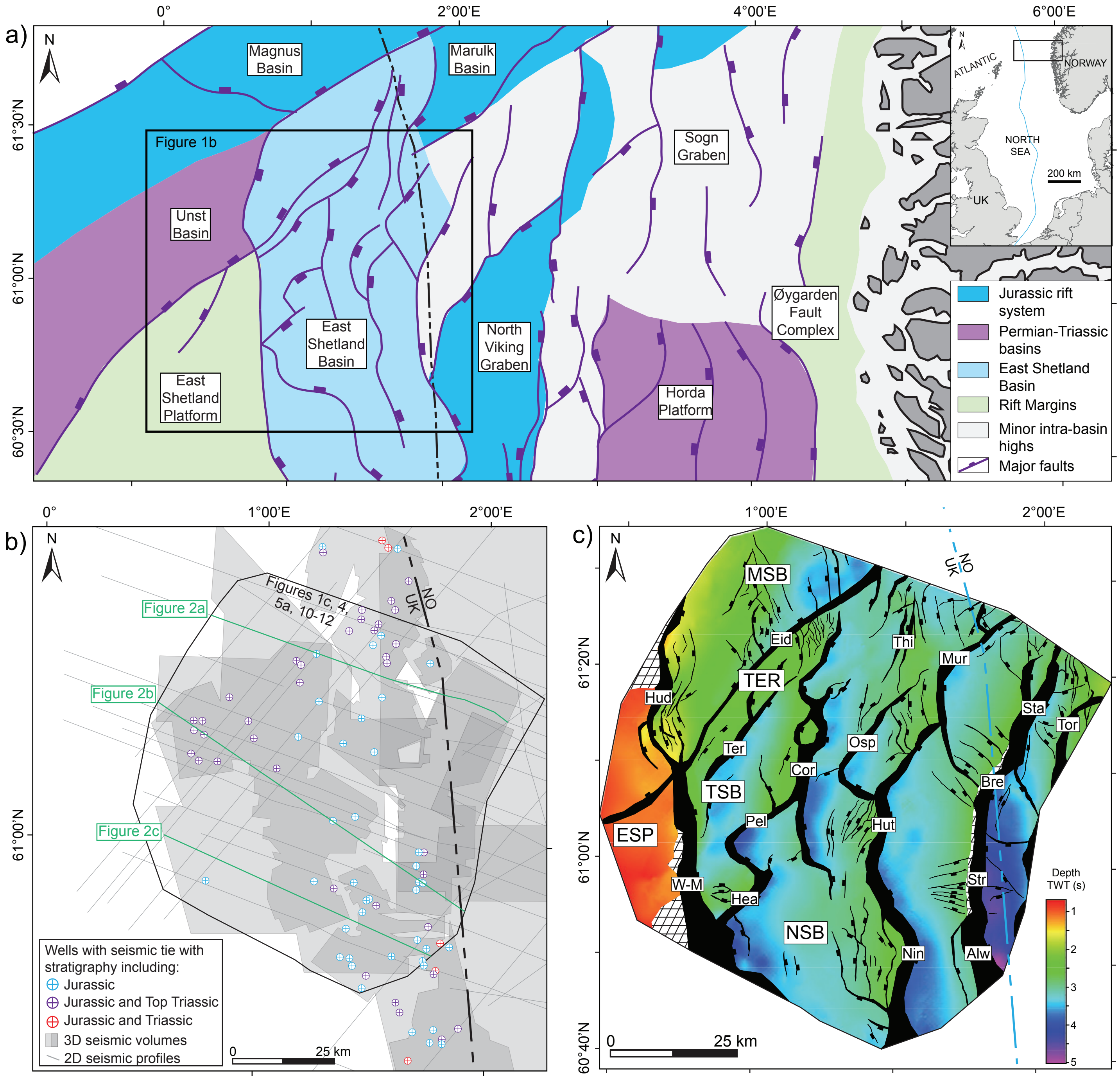

Figure 1. a) Major tectonic elements of the northern North Sea (after Færseth, 1996; Bell et al., 2014). b) Outlines of dataset used for this study. All wells are tied to the seismic data and contain stratigraphic data for the Jurassic (blue), Jurassic and Top Triassic (purple), and Jurassic and Triassic (red). c) Time-structure map of the Top Lunde Formation with major structural elements and faults: Alw = Alwyn Fault, Bre = Brent Fault, Cor = Cormorant Fault, Eid = Eider Fault, ESP = East Shetland Platform, Hea = Heather Fault, Hud = Hudson Fault, Hut = Hutton Fault, MSB = Magnus sub-basin, Mur = Murchison Fault, Nin = Ninian, NSB = Ninian sub-basin, Osp = Osprey Fault, Pel = Pelican Fault, Sta = Statfjord Fault, Str = Strathspey, TER = Tern-Eider Ridge, Ter = Tern Fault, TSB = Tern sub-basin, Thi = Thistle Fault, Tor = Tordis Fault, W–M = West Margin Fault. The faults and structural features are named after the adjacent hydro-carbon bearing fields. Modified after Claringbould et al., 2017.

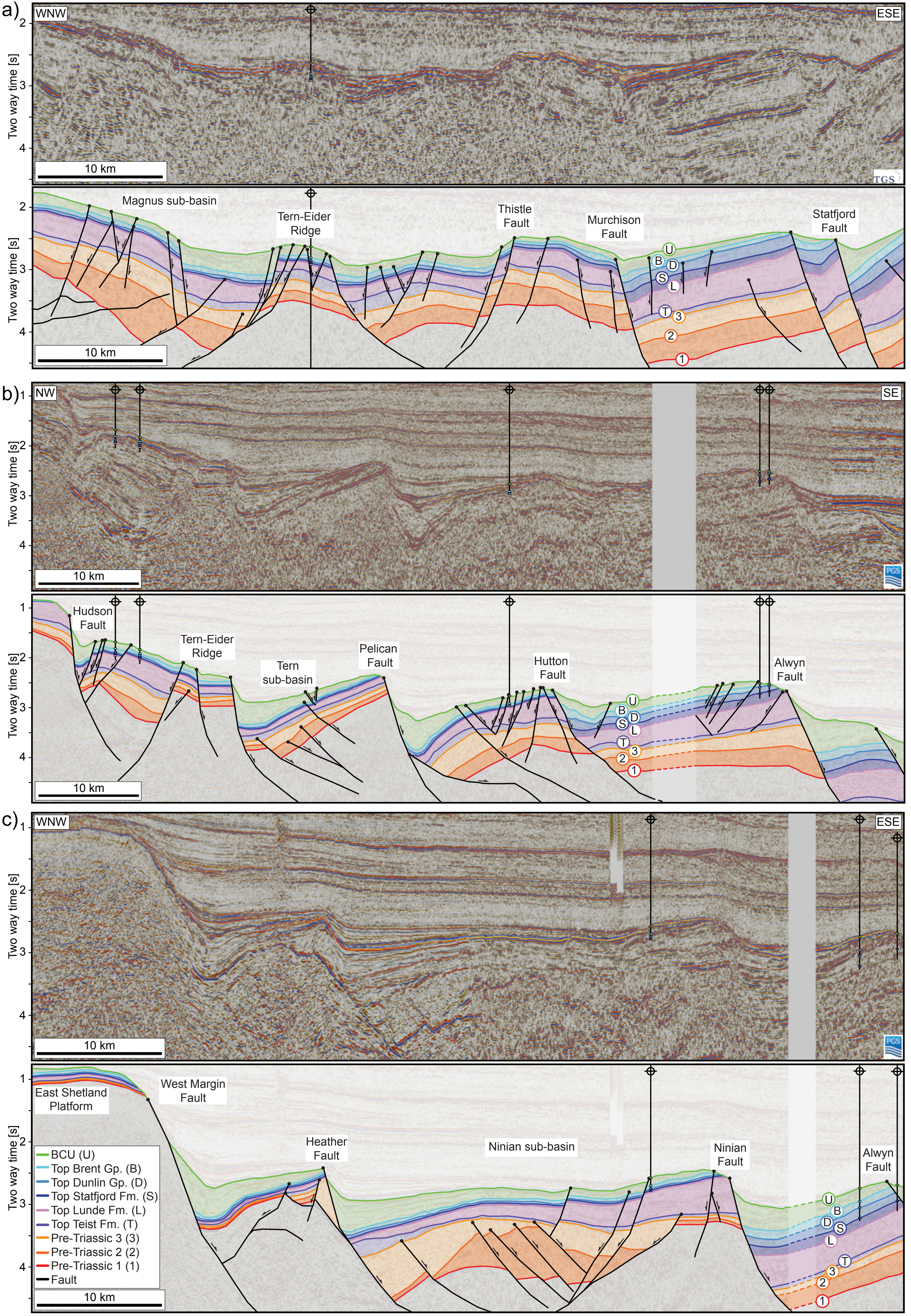

Figure 2. Uninterpreted and interpreted 2D time-migrated seismic reflection profiles crossing the study area in the a) north, b) centre, and c) south. The seismic profiles including well penetrations and major faults and structural features. See Figure 1b for locations. Modified after Claringbould et al. (2017).

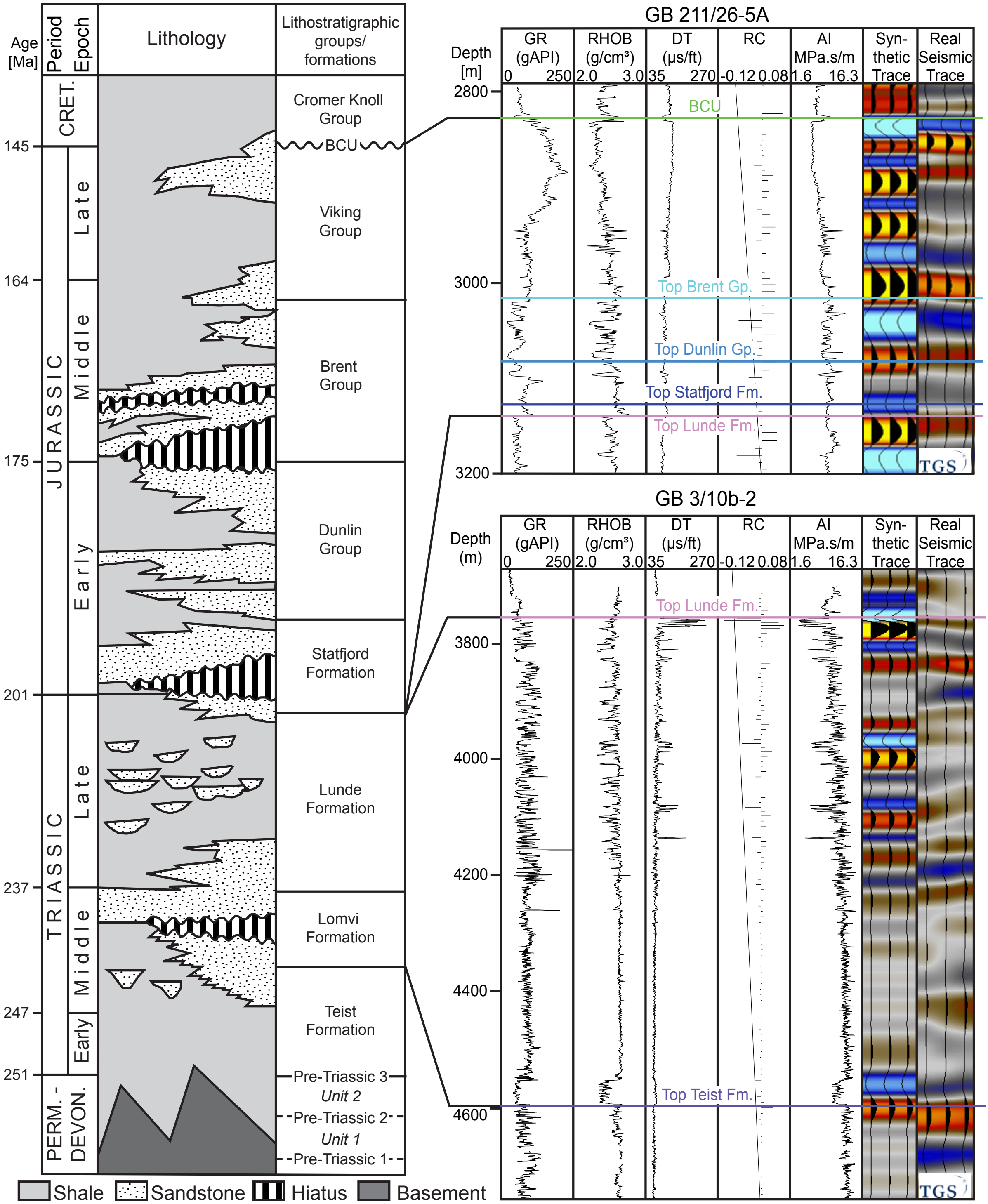

Figure 3. Stratigraphic column of the pre-Triassic-to-Cretaceous in the East Shetland Basin showing lithology (after Færseth, 1996), lithostratigraphic groups/formations and ages, and the interpreted horizons and synthetic well ties (modified after Claringbould et al., 2017). Depth = TVD, GR = Gamma Ray, RHOB = Density, DT = Sonic, RC = Reflection Coefficient, AI = Acoustic Impedance.

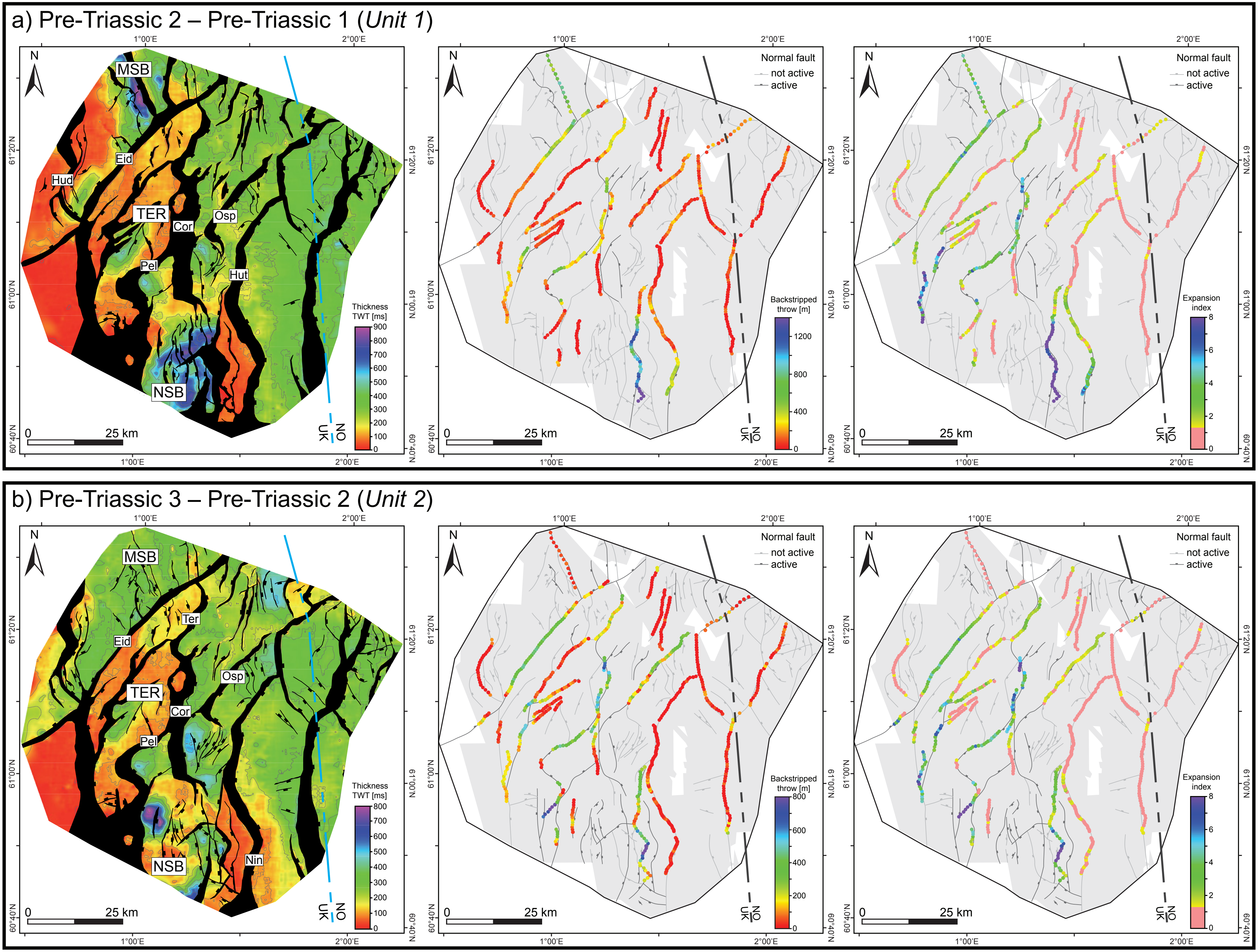

Figure 4. Isochrons overlain by fault polygons that offset the top surface (left) with line drawing of faults over outline of 3D seismic data coverage (grey polygons) overlain by the calculated backstripped throw (middle), and expansion index (right) during the deposition of a) Unit 1, b) Unit 2, c) Teist Formation, d) Lomvi and Lunde formations, e) Statfjord Formation, f) Dunlin Group, g) Brent Group, and h) Viking Group. Isochron colours are based on the maximum and minimum thickness value in ms TWT per isochron. Contour interval on all the isochrons is 100 ms TWT. Hatched areas show locations where the upper horizon is eroded. See caption of Figure 1 for abbreviated fault and structural features names. See Figure 1c for location.

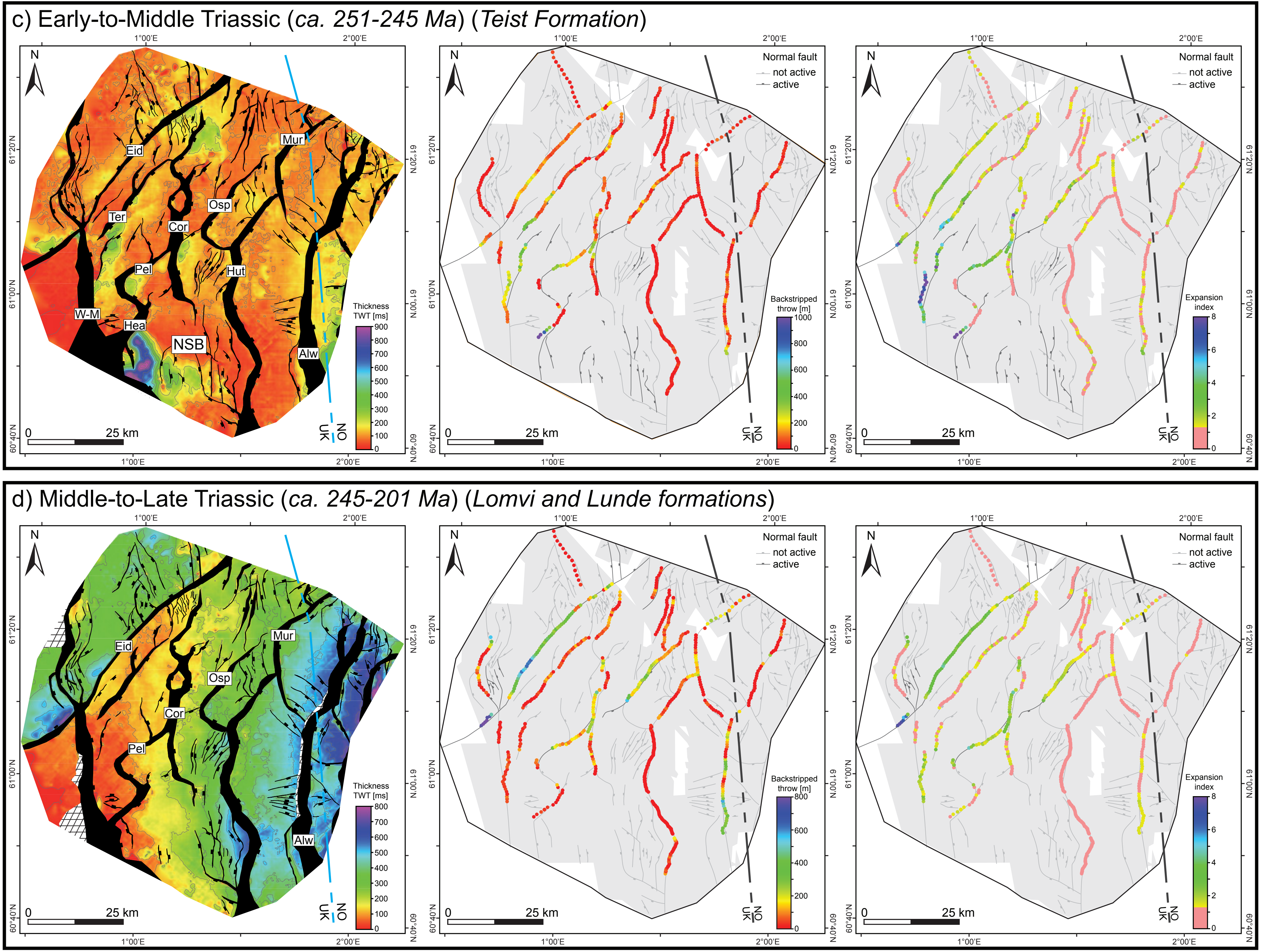

Figure 4. *-continued-*

e) Latest Triassic-to-Early Jurassic (*ca. 201-192 Ma*) (*Statfjord Formation*)

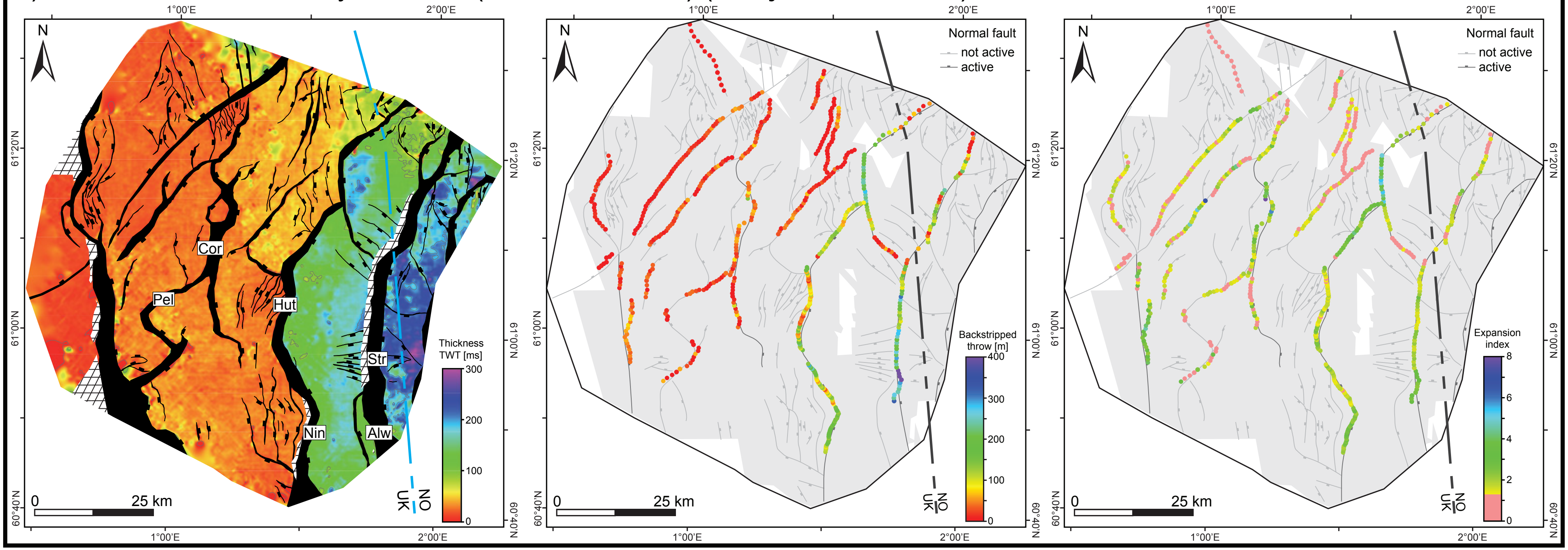

f) Early Jurassic (*ca. 192-175 Ma*) (*Dunlin Group*)

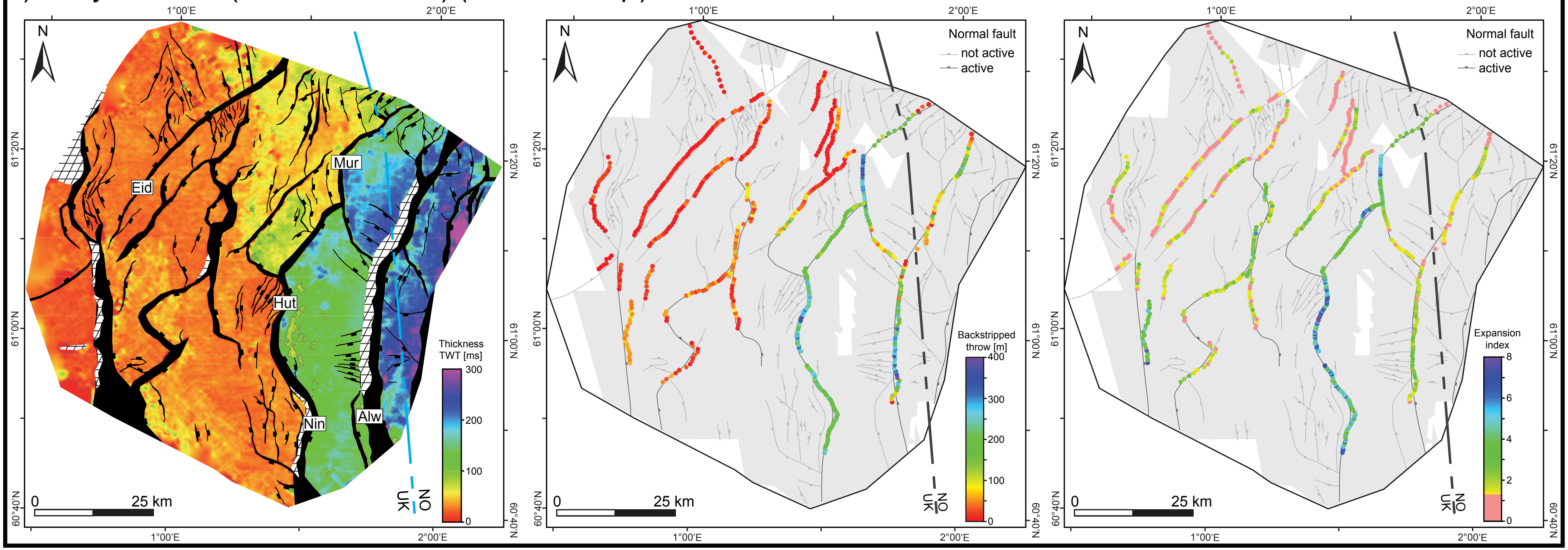

Figure 4. *-continued-*

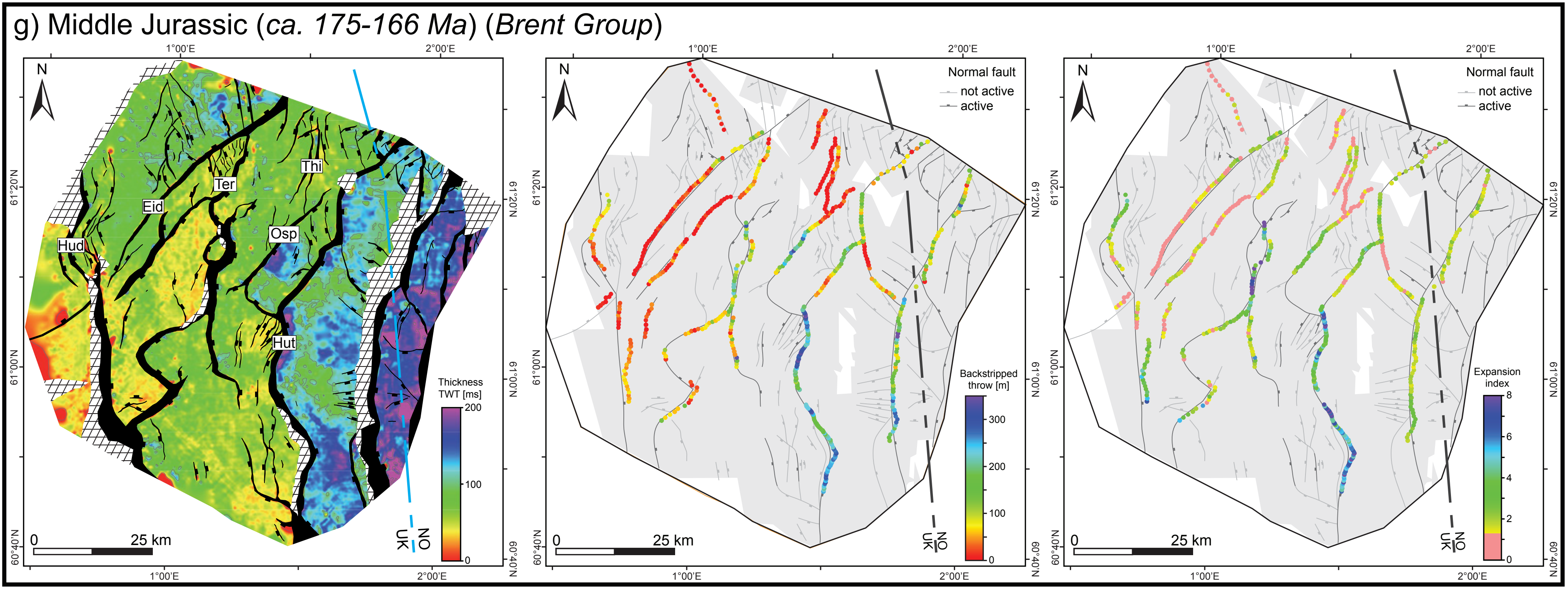

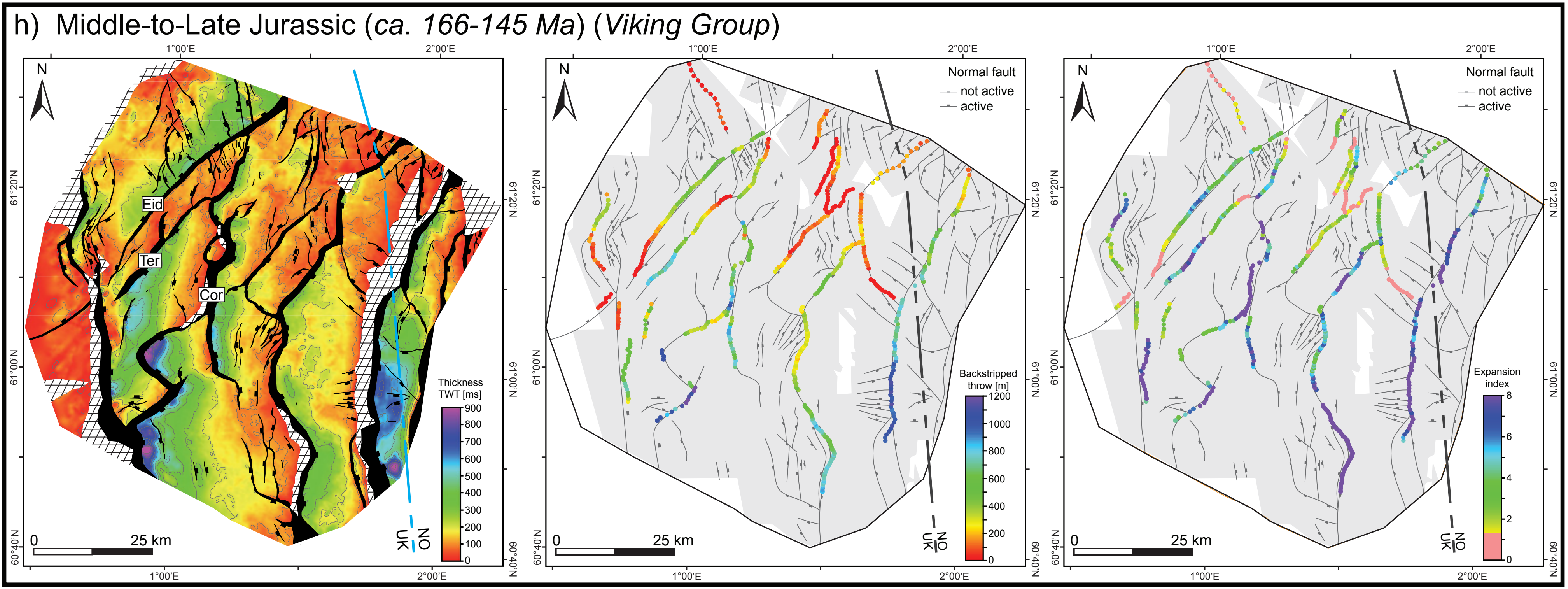

Figure 4. *-continued-*

a) Location of the measurements, transect lines and regions

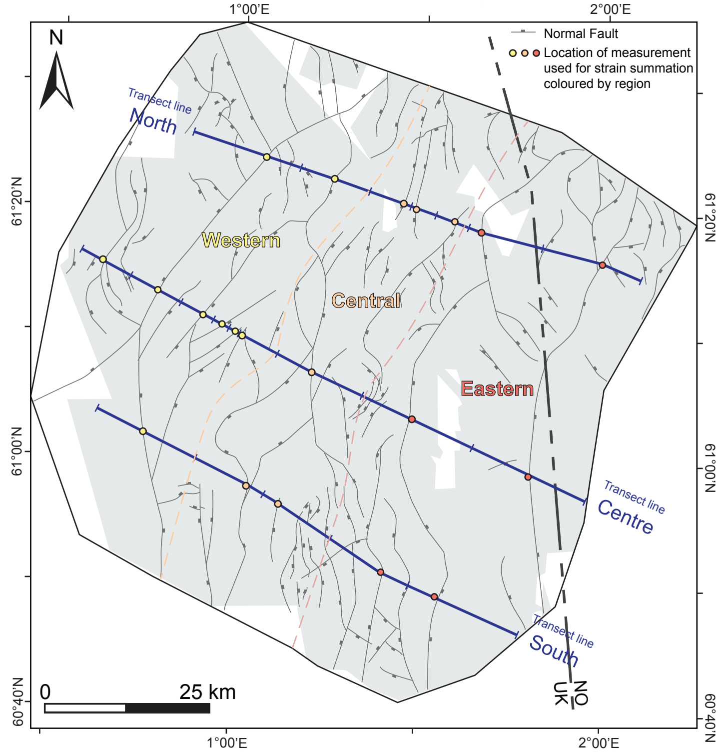

b) Summation of extension [m] for each time period per region and transect line

Time [Ma]	Age (*Formation/Group*)	Region: Western (n=9)	Region: Central (n=6)	Region: Eastern (n=6)	**Average**	Transect line: North (n=7)	Transect line: Centre (n=9)	Transect line: South (n=5)
145	Middle-to-Late Jurassic (*Viking Group*)	1849	1908	1844	**1867**	1245	2350	2007
166	Middle Jurassic (*Brent Group*)	232	179	692	**368**	214	544	346
175	Early Jurassic (*Dunlin Group*)	84	150	599	**278**	316	392	126
192	Latest Triassic-to-Early Jurassic (*Statfjord Formation*)	136	111	385	**211**	266	145	222
201	Middle-to-Late Triassic (*Lomvi and Lunde formations*)	711	537	564	**604**	418	877	516
245	Early-to-Middle Triassic (*Teist Formation*)	1032	827	461	**773**	450	1369	501
>251	Pre-Triassic 3 - Pre-Triassic 2 (*Unit 2*)	1655	1420	2011	**1695**	902	1688	2495
	Pre-Triassic 2 - Pre-Triassic 1 (*Unit 1*)	1772	1765	2063	**1866**	1416	1487	2696

n is the number of locations where the extension is summed per region and transect line for each time period

c) Extension factor for each time period per transect line

Age	Transect line: North	Transect line: Centre	Transect line: South	**Average**
Middle-to-Late Jurassic (*Viking Group*)	1.018	1.028	1.028	**1.025**
Middle Jurassic (*Brent Group*)	1.003	1.031	1.027	**1.020**
Early Jurassic (*Dunlin Group*)	1.004	1.034	1.025	**1.021**
Latest Triassic-to-Early Jurassic (*Statfjord Formation*)	1.004	1.035	1.028	**1.022**
Middle-to-Late Triassic (*Lomvi and Lunde formations*)	1.006	1.046	1.034	**1.029**
Early-to-Middle Triassic (*Teist Formation*)	1.007	1.059	1.037	**1.034**
Pre-Triassic 3 - Pre-Triassic 2 (*Unit 2*)	1.013	1.022	1.037	**1.024**
Pre-Triassic 2 - Pre-Triassic 1 (*Unit 1*)	1.021	1.019	1.042	**1.028**
Total (pre-Triassic-Jurassic)	**1.078**	**1.115**	**1.139**	**1.111**

d) Extension rate [m/Myr] for each time period per transect line

Age	Transect line: North	Transect line: Centre	Transect line: South	**Average**
Middle-to-Late Jurassic (*Viking Group*)	59	112	96	**89**
Middle Jurassic (*Brent Group*)	24	60	38	**41**
Early Jurassic (*Dunlin Group*)	19	23	7	**16**
Latest Triassic-to-Early Jurassic (*Statfjord Formation*)	30	16	25	**23**
Middle-to-Late Triassic (*Lomvi and Lunde formations*)	10	20	12	**14**
Early-to-Middle Triassic (*Teist Formation*)	75	228	83	**129**

Figure 5. Strain summation across the East Shetland Basin. a) The location of each sample location along three transect lines (North, Centre, South) is shown along with the outline of the three regions (Western, Central, and Eastern). b) Summation of extension [m] for each time period. Values are subdivided per region, average, and transect lines. c) Extension factor per period along each transect line and average, and total pre-Triassic-Jurassic extension factors. d) Triassic-Jurassic extension rate [m/Myr] for each period along each transect line and average across the basin. Darker shades represent relative larger values.

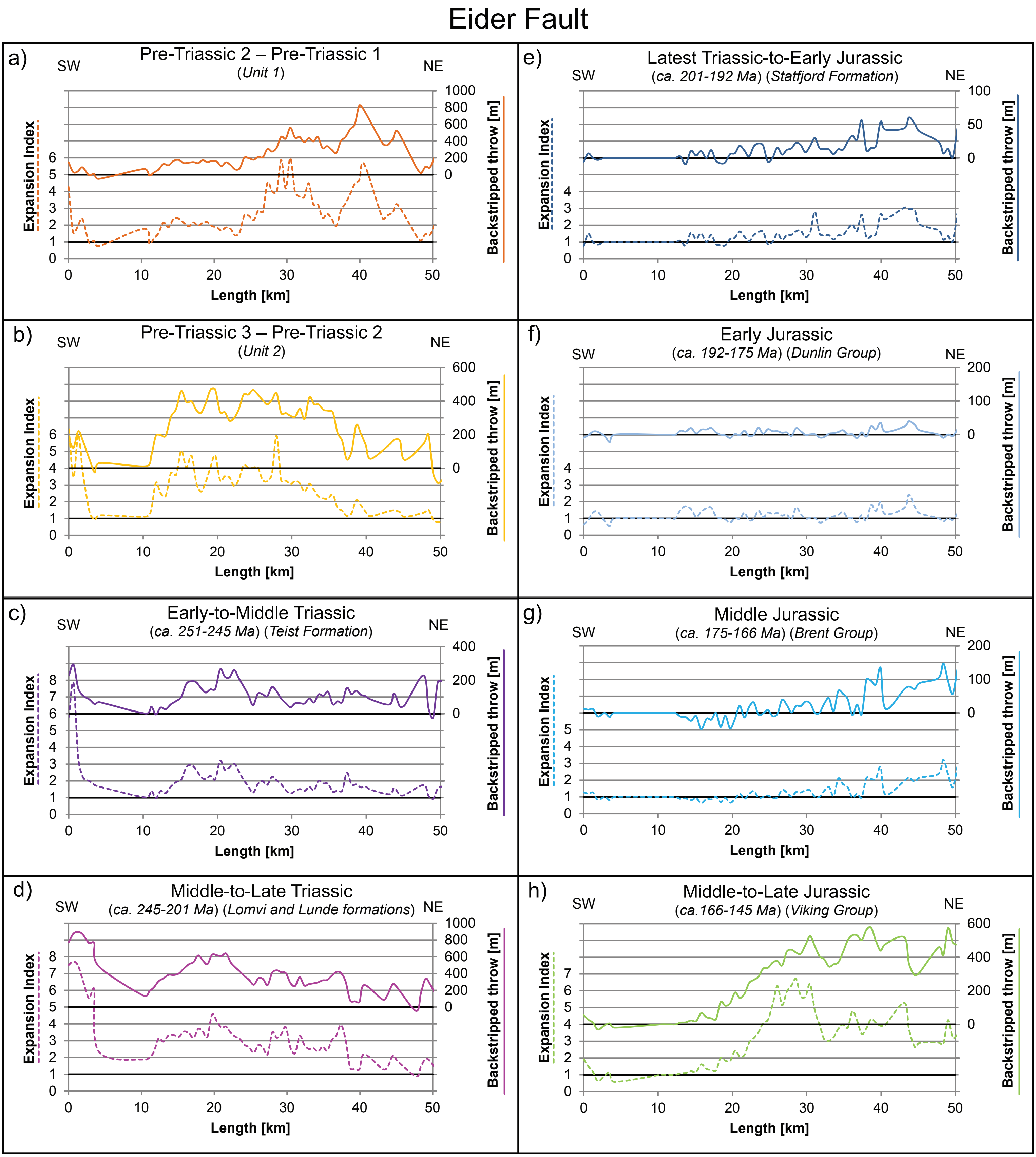

Figure 6. Expansion index (dashed) and backstripped throw [m] (continuous) along the Eider Fault per time interval: a) Pre-Triassic 2 – Pre-Triassic 1, b) Pre-Triassic 3 – Pre-Triassic 2, c) Early-to-Middle Triassic, d) Middle-to-Late Triassic, e) Latest Triassic-to-Early Jurassic, f) Early Jurassic, g) Middle Jurassic, and h) Middle-to-Late Jurassic. See Figure 10 for location of Eider Fault.

Ninian-Hutton Fault

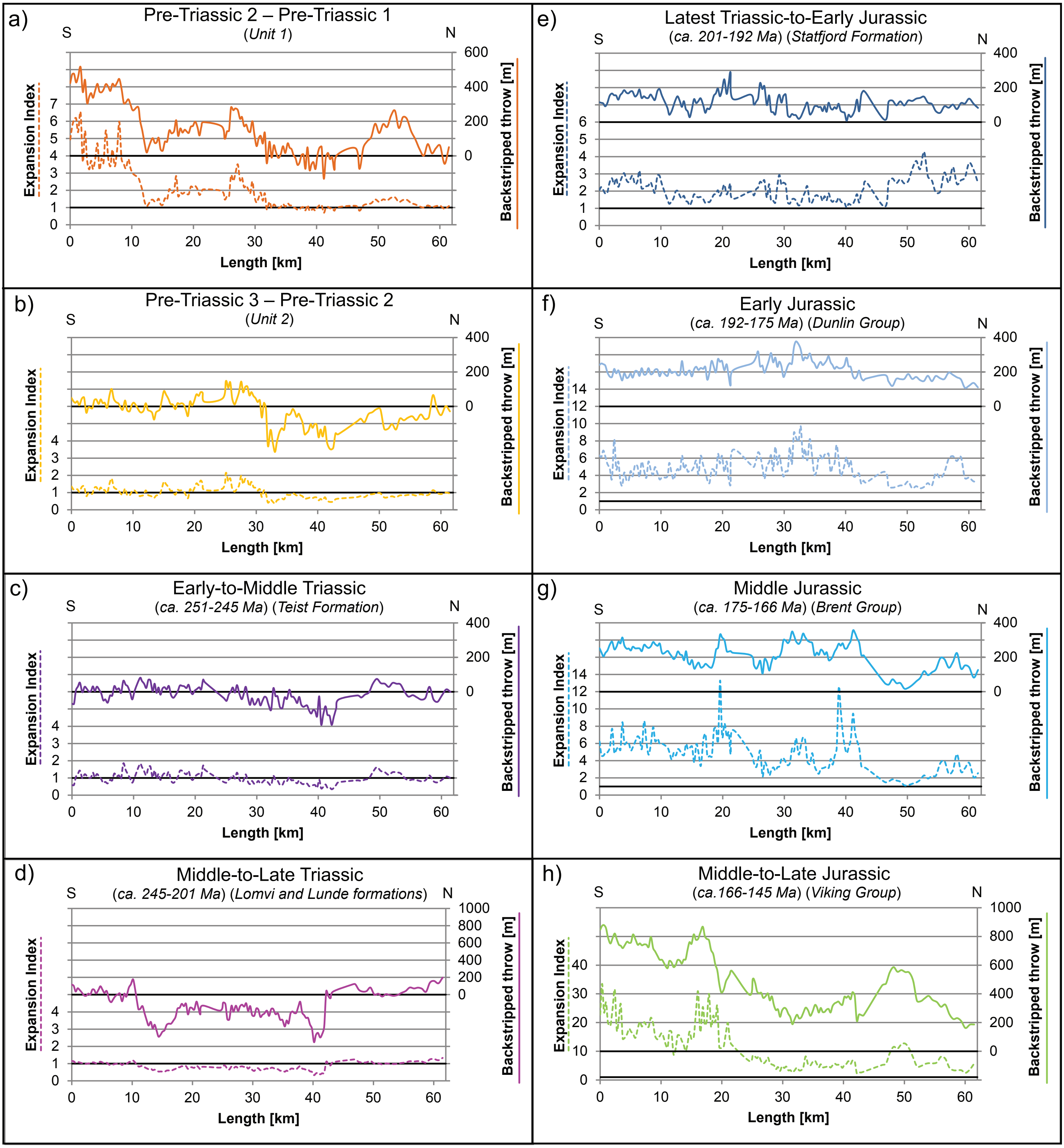

Figure 7. Expansion index (dashed) and backstripped throw [m] (continuous) along the Ninian-Hutton Fault per time interval: a) Pre-Triassic 2 – Pre-Triassic 1, b) Pre-Triassic 3 – Pre-Triassic 2, c) Early-to-Middle Triassic, d) Middle-to-Late Triassic, e) Latest Triassic-to-Early Jurassic, f) Early Jurassic, g) Middle Jurassic, and h) Middle-to-Late Jurassic. See Figure 10 for location of Ninian-Hutton Fault.

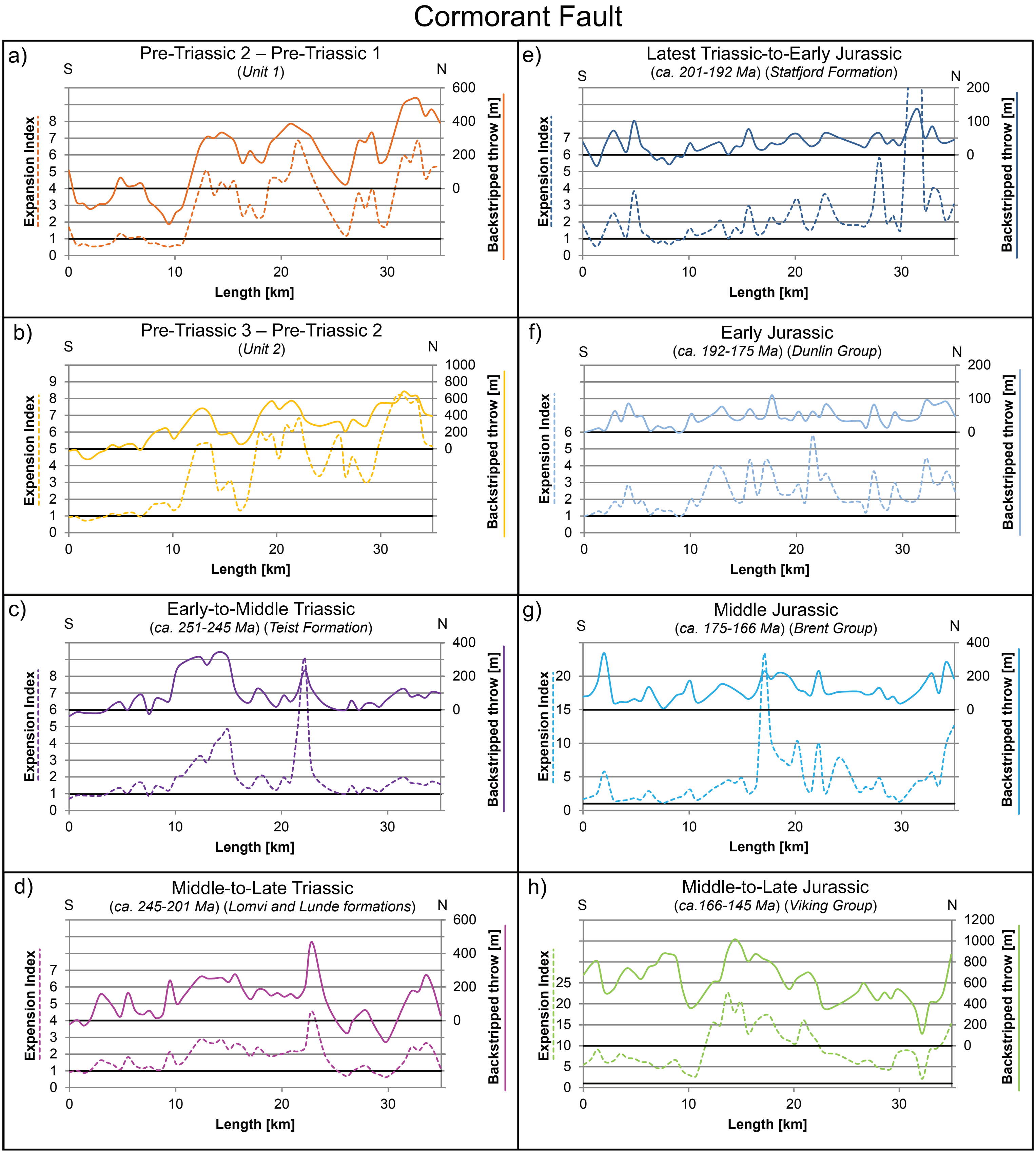

Figure 8. Expansion index (dashed) and backstripped throw [m] (continuous) along the Cormorant Fault per time interval: a) Pre-Triassic 2 – Pre-Triassic 1, b) Pre-Triassic 3 – Pre-Triassic 2, c) Early-to-Middle Triassic, d) Middle-to-Late Triassic, e) Latest Triassic-to-Early Jurassic, f) Early Jurassic, g) Middle Jurassic, and h) Middle-to-Late Jurassic. See Figure 10 for location of Cormorant Fault.

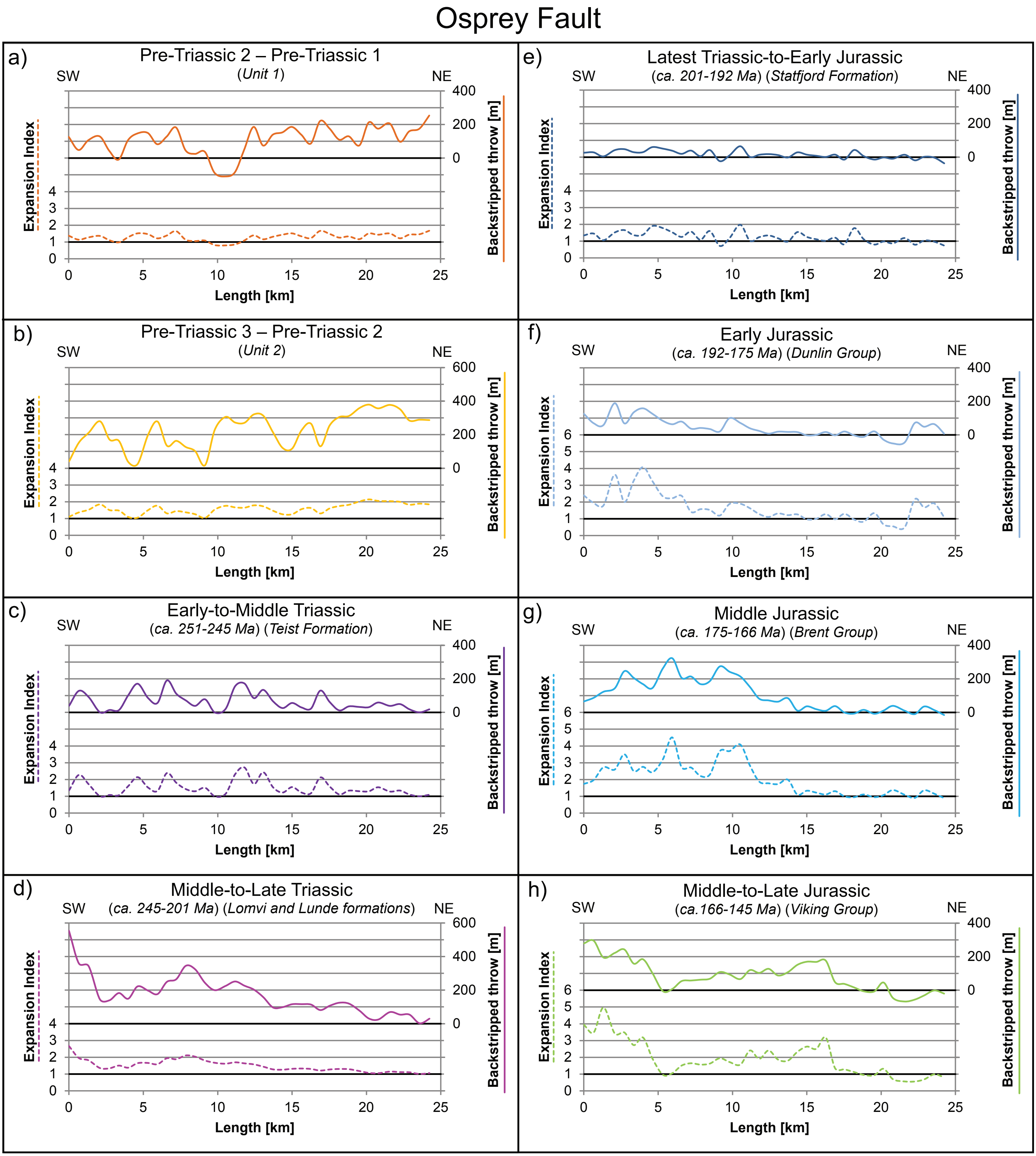

Figure 9. Expansion index (dashed) and backstripped throw [m] (continuous) along the Osprey Fault per time interval: a) Pre-Triassic 2 – Pre-Triassic 1, b) Pre-Triassic 3 – Pre-Triassic 2, c) Early-to-Middle Triassic, d) Middle-to-Late Triassic, e) Latest Triassic-to-Early Jurassic, f) Early Jurassic, g) Middle Jurassic, and h) Middle-to-Late Jurassic. See Figure 10 for location of Osprey Fault.

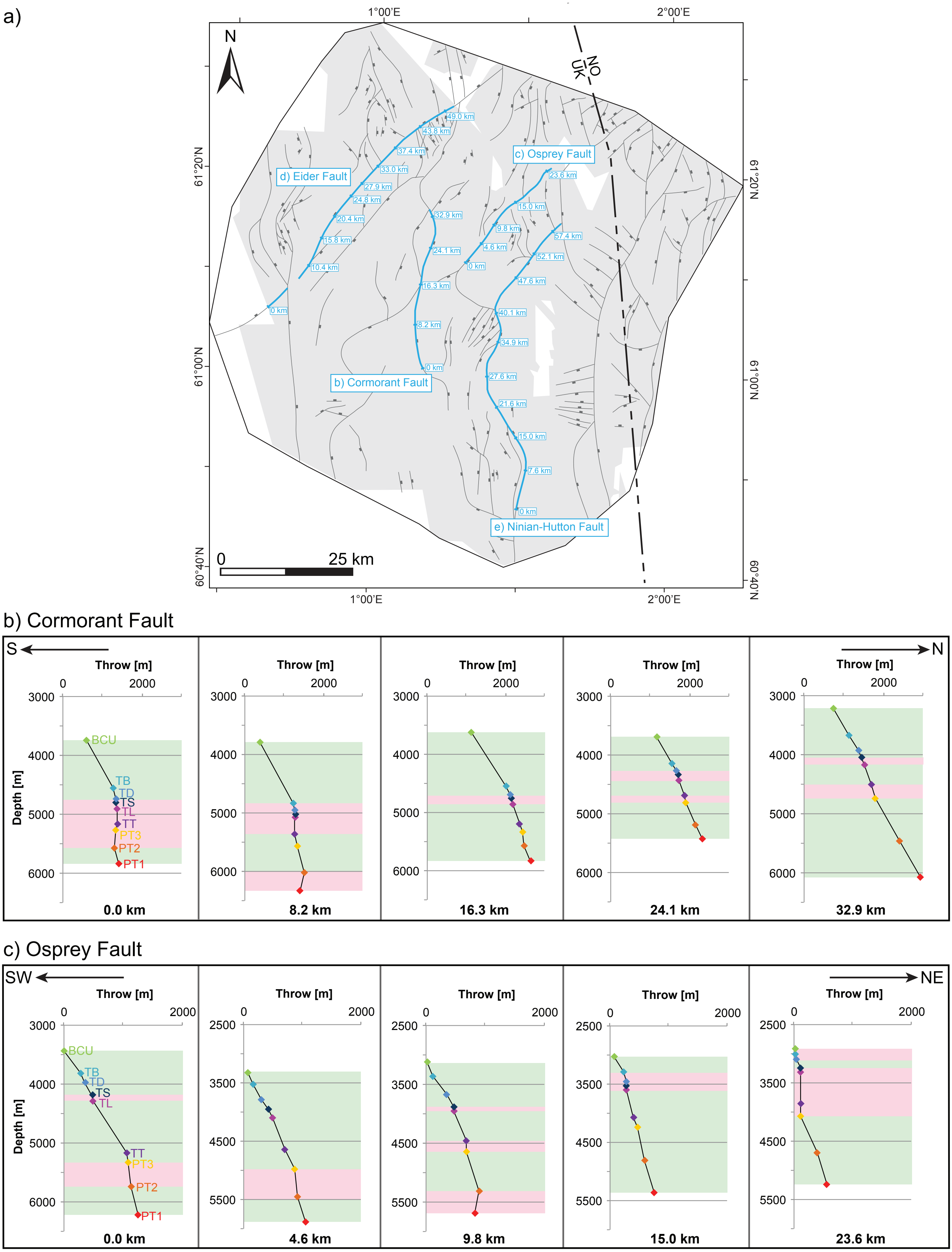

Figure 10. a) Map of the East Shetland Basin, showing faults that cross the Top Brent horizon. The grey outlines the seismic data coverage. The location of the detailed analysed faults are highlighted in blue with the locations of throw-depth plots marked along the length of the fault: b) Cormorant Fault, c) Osprey Fault, d) Eider Fault, and e) Ninian-Hutton Fault. Green shaded areas are interpreted to represent fault growth activity, while red shaded areas represent inactive fault growth. BCU = Base Cretaceous Unconformity, TB = Top Brent Group, TD = Top Dunlin Group, TS = Top Statfjord Formation, TL = Top Lunde and Lomvi formations, TT = Top Teist Formation, PT3 = Top Unit 2, PT2 = Top Unit 1, PT1 = Bottom Unit 1.

d) Eider Fault

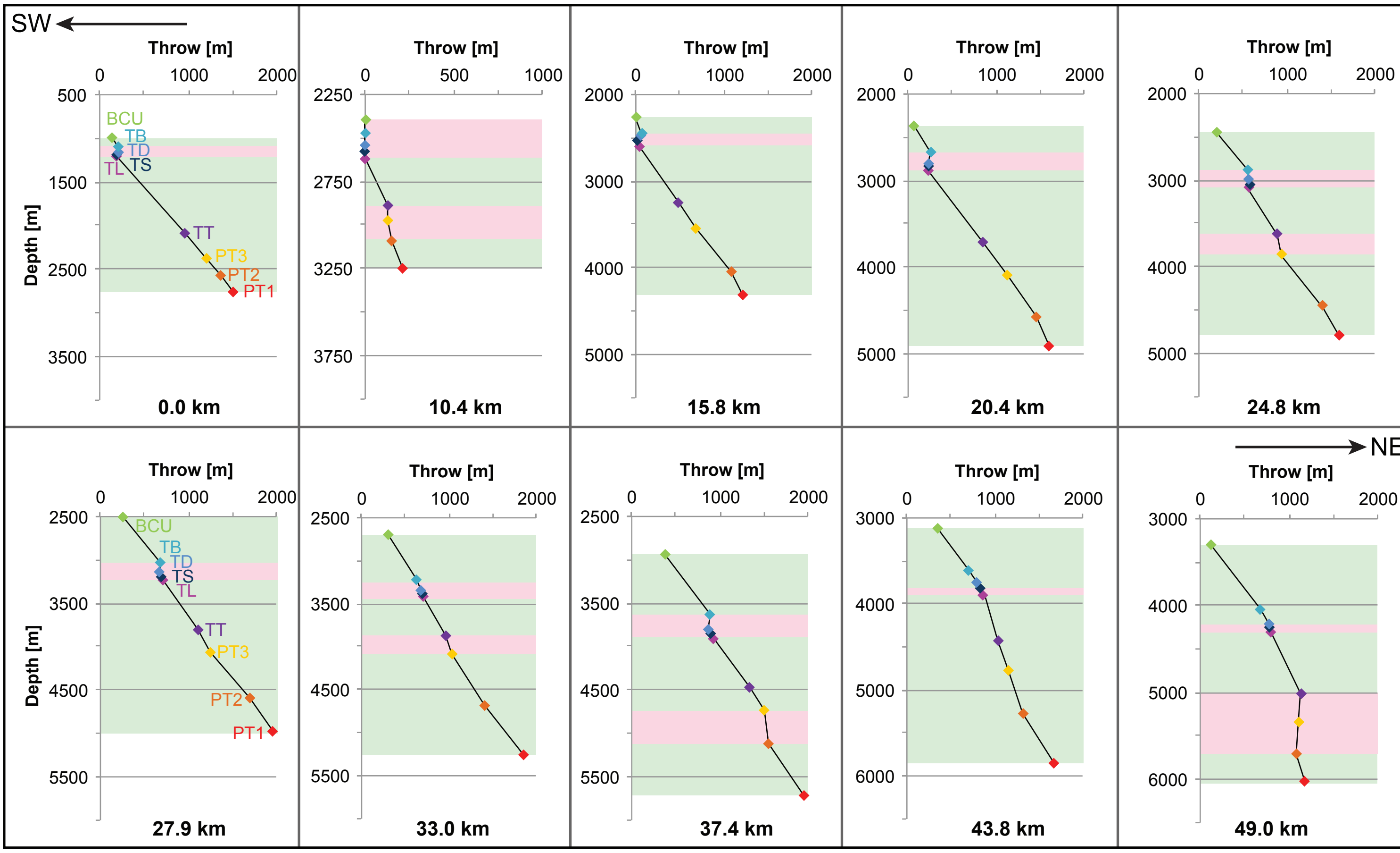

e) Ninian-Hutton Fault

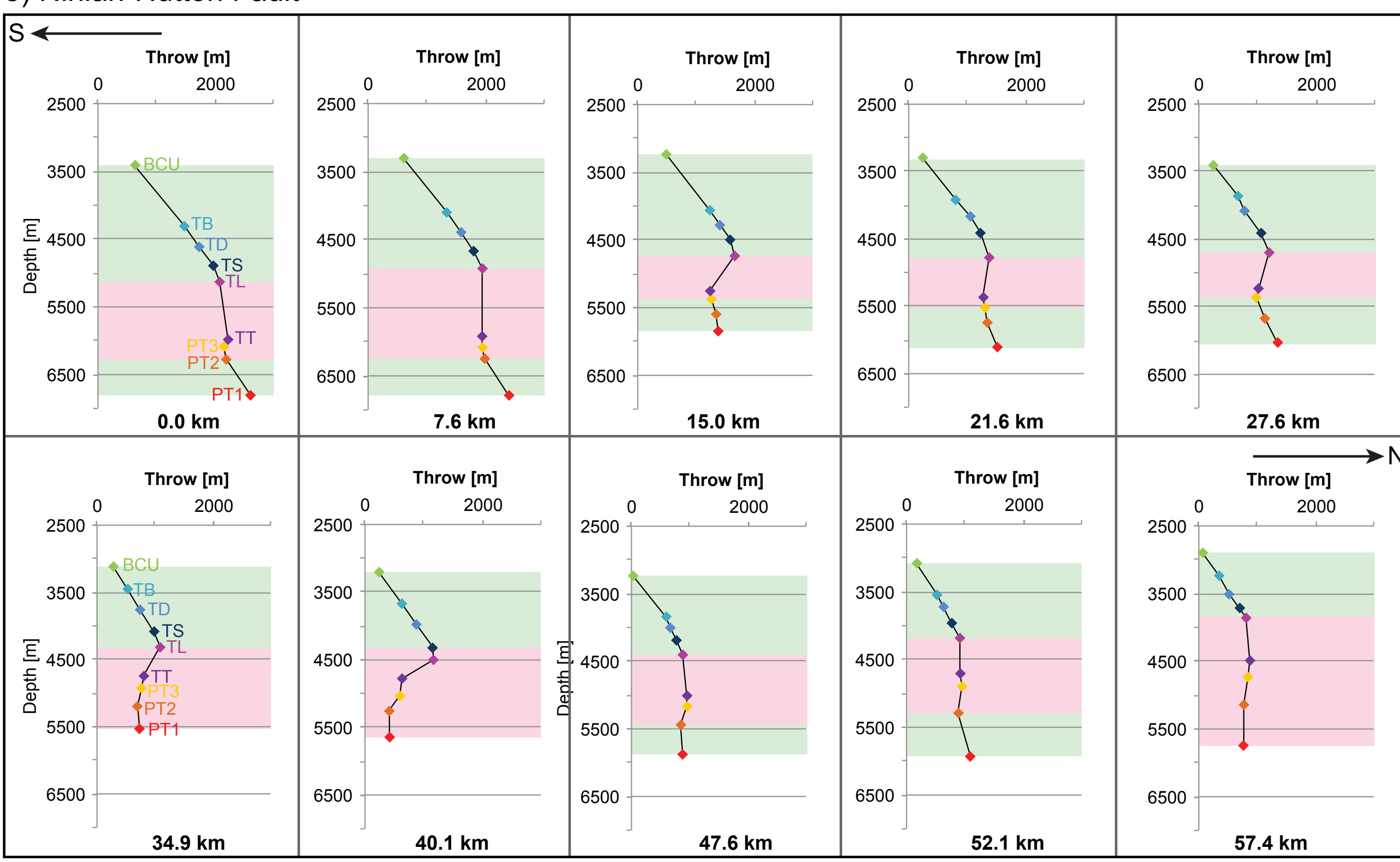

Figure 10. *-continued-*

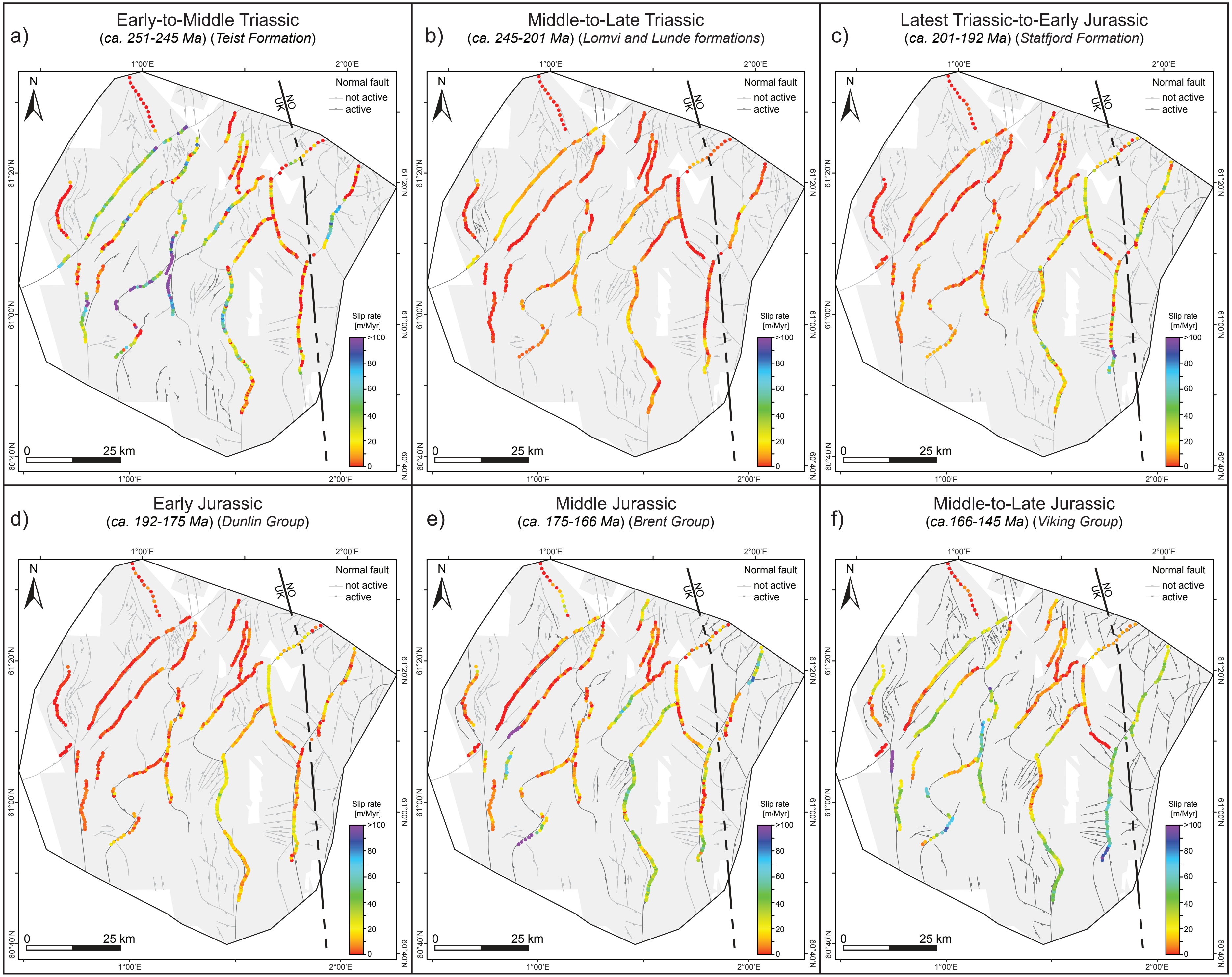

Figure 11. Line drawing of faults over outline of 3D seismic data coverage (grey polygons) overlain by Triassic-Jurassic fault slip rates across the East Shetland Basin per time interval: a) Early-to-Middle Triassic, b) Middle-to-Late Triassic, c) Latest Triassic-to-Early Jurassic, d) Early Jurassic, e) Middle Jurassic, and f) Middle-to-Late Jurassic.

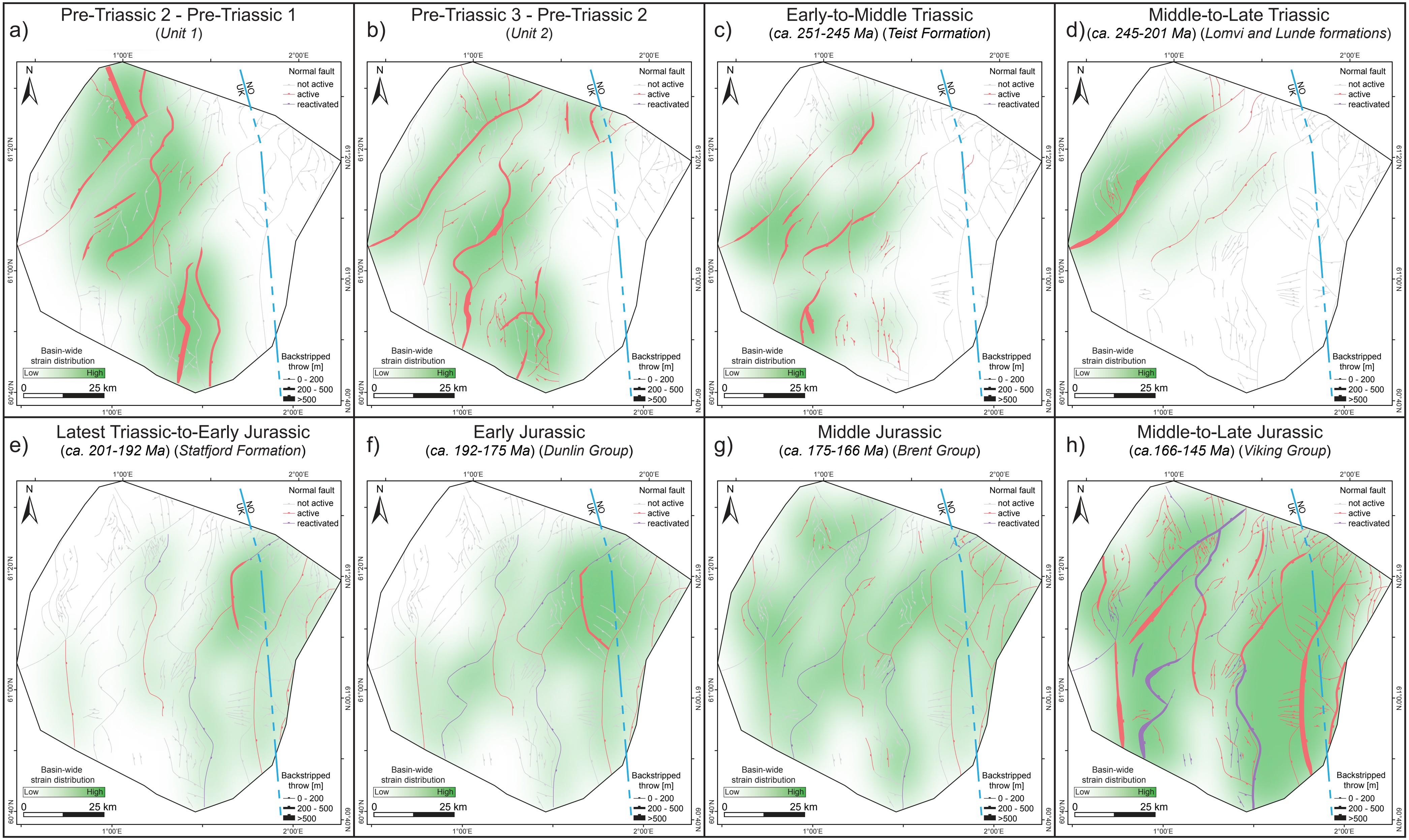

Figure 12. Basin-wide strain distribution across the East Shetland Basin per time interval: a) Pre-Triassic 2 – Pre-Triassic 1, b) Pre-Triassic 3 – Pre-Triassic 2, c) Early-to-Middle Triassic, d) Middle-to-Late Triassic, e) Latest Triassic-to-Early Jurassic, f) Early Jurassic, g) Middle Jurassic, and h) Middle-to-Late Jurassic.

Supporting Information for

Complex strain partitioning and heterogeneous extension rates during early rifting in the East Shetland Basin, northern North Sea

Johan S. Claringbould[1,2], Rebecca E. Bell[2], Christopher A-L. Jackson[2], Robert L. Gawthorpe[3], Tore Odinsen[4]

[1]Earthquake Research Institute, The University of Tokyo, 1-1-1 Yayoi, Bunkyo-ku, Tokyo, 113-0032, Japan, [2]Basins Research Group (BRG), Department of Earth Science and Engineering, Imperial College, London, SW7 2BP, UK, [3]Department of Earth Science, University of Bergen, Allégaten 41, 5007 Bergen, Norway, [4]Equinor ASA, Sandslihaugen 30, 5254 Sandsli, Norway

Contents of this file

Introduction

This supporting information contains supplemental material for *3.3 Fault array analyses* and references, and includes a detailed data availability statement.

Supplemental material

S1. Expansion index and backstripped throw

The expansion index represents the relative vertical stratal thickness ratio between the hanging wall and adjacent footwall (i.e., the hanging wall vertical stratal thickness divided by the footwall vertical stratal thickness). Where the expansion index is >1, syn-depositional fault activity is interpreted to have occurred, and when the expansion index ≤1, the fault is interpreted to be inactive during deposition of that stratal unit (Thorsen, 1963).

Fault throw backstripping involves the sequential subtraction of throw across successively older horizons: this is equivalent to the difference in across-fault vertical stratal thickness for each time period (i.e., the hanging wall vertical stratal thickness minus the adjacent footwall vertical stratal thickness) (e.g., Jackson et al., 2017). As we are investigating how strain is distributed across the basin we are using the original method for fault throw backstripping, rather than the modified method that is more appropriate when one is concerned with the detailed growth and linkage of individual segments comprising the larger fault systems (Jackson et al., 2017). Our calculated backstripped throw values are related to the accompanied expansion indices and are able to put them in perspective if the backstripped throw value is below the vertical seismic resolution (~28 m) (Claringbould, 2015): e.g., when the backstripped throw is below the vertical seismic resolution, a high expansion index can be the result of a picking error. Similar to the expansion indices, the backstripped throw values are interpreted to indicate a quantitative measure that shows along strike variation in syn-depositional fault activity.

S2. Extension, extension rate, and extension factor

Extension, extension rate, and extension factor are commonly used to analyse the strain distribution history across basins (e.g., Færseth, 1996; Odinsen et al., 2000; Bell et al., 2011). Three, transect lines are drawn striking ~NW-SE across the basin (North, Centre, South), approximately orthogonally crossing major structural elements. We calculate the upper-crustal extension, extension rate, and extension factor at each location where one of the three transect lines crosses one of the 34 analysed faults within the fault array.

The upper-crustal extension at these points represents the amount of fault heave that developed at the fault during a certain time period. We calculate extension using the backstripped displacement and maximum fault dip angle. We use the maximum fault angle even though the listric nature of the analysed fault is limited: the average difference between the maximum and minimum fault dip angle measured at each sample location along the analysed faults is 13.2 degrees, with a maximum of 18.7 degrees. We assume that the maximum fault dip angle is most representative of the fault dip angle during fault growth at an analysed time period. Furthermore, using the maximum fault angle also limits the potential effect of footwall erosion, which decreases the fault dip updip. The maximum fault dip angle is subsequently corrected for block-rotation if the fault is located in a rotated hanging wall of a neighbouring fault, or when the fault dip angle is affected by younger fault cross-cutting the analysed fault.

Per time period, the extension calculated at each sample location is summed along the three transects (North, Centre, South) and, additionally, within the three regions (Western, Central, and Eastern). Subdividing the amount of extension per transect line and by region allows us to investigate the distribution of strain across the East Shetland Basin over time. Subsequently, the extension rate per transect line is determined for the Triassic and Jurassic time periods to analyse the absolute strain distribution history. Since lithostratigraphic horizons do not necessarily represent chronostratigraphic surfaces (i.e. absolute time-lines), the absolute ages used to estimate the extension rate are based on the average absolute age of the lithostratigraphic boundaries from the wells. The absolute ages of the lithostratigraphic boundaries based on biostratigraphic analyses of the well data. Due to the large extent of the East Shetland Basin (~10.000 km2) the average ages have a maximum difference of ±4 Myr across the fault array, but the time interval of deposition is relatively similar within the basin (±2 Myr). Due to the large time interval of analysis (~150 Myr), we consider using the average absolute age for the lithostratigraphic boundaries to be sufficient to analyse strain accumulation across the entire fault array.

Lastly, the extension factor is calculated along each transect line per time period to constrain the relative strain distribution across the fault array during rifting. During rifting the basin extends along the active faults in the upper-crust, increasing the fault heaves and therefore increasing the initial length of the transect line. The extension factor represents relative length ratio of the transect line between two time-horizons: younger over older transect line length. The calculated extension factors are >1, as the length of the transect line increases over time due to rifting (e.g., Bell et al., 2011). Similar to throw and displacement backstripping, the length of the transect line is based on the sequential subtracting of extension amounts of younger time-horizons and the extension of the analysed time-horizon from the current transect length at each point where it crosses an analysed fault.

S3. Throw-depth plots

Throw-depth plots can be used to determine the depth at which faults nucleate and how they propagate vertically (e.g., Hongxing & Anderson, 2007; Jackson & Rotevatn, 2013; Bell et al., 2014; Reeve et al., 2015; Jackson et al., 2017). Hongxing and Anderson (2007) show that throw-depth plots in which throw is constant or decreases with depth (and thus horizon age) are typically associated with post-depositional faulting, whereas, throw-depth plots in which throw increases with depth and horizon age are indicative of syn-depositional faulting. In this study we are concerned with the varying strain accommodation along the fault (i.e. along strike fault growth evolution). If the character of the throw-depth profiles (i.e., the geometry of the throw-depth plot) are similar along the length of a fault, a laterally consistent growth evolution is assumed (e.g., Jackson & Rotevatn, 2013). However, if throw-depth profiles vary in geometry (i.e., gradient variation between the same horizon-nodes) along the length of the fault, the fault growth is assumed to be laterally diachronous, and therefore reflecting heterogeneous strain distribution across the basin over time.

S4. Fault slip rate

Similar to the expansion indices and backstripped throw values, we calculate fault slip rate along each major fault for every time period, with the exception of the pre-Triassic units as the age of these is unconstrained (Units 1 and 2) (Figure 11). The fault slip rate represents the backstripped displacement over time in m/Myr, and shows the variation in strain distribution along strike of each major fault and across the fault array as rifting progressed. Similar to backstripped throw, displacement backstripping involves the sequential subtractions of displacements on successively older horizons; where the displacement is calculated using the throw and heave of a faulted horizon (e.g., Childs et al., 1993; Ten Veen & Kleinspehn, 2000; Walsh et al., 2002; Taylor et al., 2004, 2008; Bell et al., 2014; Jackson et al., 2017). Similar to the extension rates the absolute ages used to estimate the fault slip rates are based on the average absolute age of the lithostratigraphic boundaries across the East Shetland Basin (see Supplemental material section 2). Fault slip rates are displayed in Figure 11 and since only a few measurements are >100 m/Myr the colour ranges from 0 to >100 m/Myr. Of the 634 measurements made for each time period, 29 (maximum of 212 m/Myr, Teist Formation), 12 (maximum of 333 m/Myr, Brent Group), and 9 (maximum of 127 m/Myr, Viking Group), are >100 m/Myr.

References

Bell, R. E., Jackson, C. A-L., Whipp, P. S., & Clements, B. (2014). Strain migration during multiphase extension: Observations from the northern North Sea. *Tectonics*, *33*(10), 1936–1963. https://doi.org/10.1002/2014TC003551

Bell, R. E., McNeill, L. C., Henstock, T. J., & Bull, J. M. (2011). Comparing extension on multiple time and depth scales in the Corinth Rift, Central Greece. *Geophysical Journal International*, *186*(2), 463–470. https://doi.org/10.1111/j.1365-246X.2011.05077.x

Childs, C., Easton, S. J., Vendeville, B. C., Jackson, M. P. A., Lin, S. T., Walsh, J. J., & Watterson, J. (1993). Kinematic analysis of faults in a physical model of growth faulting above a viscous salt analogue. *Tectonophysics*, *228*(3-4), 313–329. https://doi.org/10.1016/0040-1951(93)90346-L

Claringbould, J. S. (2015). *Structural and stratigraphic expression of multiphase extension in rift basins*, (Doctoral dissertation). Retrieved from Spiral (http://hdl.handle.net/10044/1/51557). London, UK: Imperial College London.

Færseth, R. B. (1996). Interaction of Permo-Triassic and Jurassic extensional fault-blocks during the development of the northern North Sea. *Journal of the Geological Society*, *153*(6), 931–944. https://doi.org/10.1144/gsjgs.153.6.0931

Hongxing, G., & Anderson, J. K. (2007). Fault throw profile and kinematics of Normal fault: conceptual models and geologic examples. *Geological Journal of China Universities*, *13*, 75-88.

Jackson, C. A-L., Bell, R. E., Rotevatn, A., & Tvedt, A. B. (2017). Techniques to determine the kinematics of synsedimentary normal faults and implications for fault growth models. *Geological Society, London, Special Publications*, *439*(1), 187–217. https://doi.org/10.1144/SP439.22

Jackson, C. A-L., & Rotevatn, A. (2013). 3D seismic analysis of the structure and evolution of a salt-influenced normal fault zone: a test of competing fault growth models. *Journal of Structural Geology*, *54*, 215–234. https://doi.org/10.1016/j.jsg.2013.06.012

Odinsen, T., Reemst, P., Van der Beek, P., Faleide, J. I., & Gabrielsen, R. H. (2000). Permo-Triassic and Jurassic extension in the northern North Sea: results from tectonostratigraphic forward modelling. *Geological Society, London, Special Publications*, *167*(1), 83–103. https://doi.org/10.1144/GSL.SP.2000.167.01.05

Reeve, M. T., Bell, R. E., & Jackson, C. A-L. (2014). Origin and significance of intra-basement seismic reflections offshore western Norway. *Journal of the Geological Society*, *171*(1), 1–4. https://doi.org/10.1144/jgs2013-020

Taylor, S. K., Bull, J. M., Lamarche, G., & Barnes, P. M. (2004). Normal fault growth and linkage in the Whakatane Graben, New Zealand, during the last 1.3 Myr. *Journal of Geophysical Research: Solid Earth*, *109*(B2). https://doi.org/10.1029/2003JB002412

Taylor, S. K., Nicol, A., & Walsh, J. J. (2008). Displacement loss on growth faults due to sediment compaction. *Journal of Structural Geology*, *30*(3), 394–405. https://doi.org/10.1016/j.jsg.2007.11.006

Thorsen, C.E. (1963). Age of growth faulting in the southeast Louisiana. *Transactions of the Gulf Coast Association of Geological Societies*, *13*, 103–110.

ten Veen, J. H., & Kleinspehn, K. L. (2000). Quantifying the timing and sense of fault dip slip: New application of biostratigraphy and geohistory analysis. Geology, 28(5), 471–474. https://doi.org/10.1130/0091-7613(2000)28<471:QTTASO>2.0.CO;2

Walsh, J. J., Nicol, A., & Childs, C. (2002). An alternative model for the growth of faults. *Journal of Structural Geology*, *24*(11), 1669–1675. https://doi.org/10.1016/S0191-8141(01)00165-1

Data availability statement

The data used for this study are publically available for download via the UK National Data Repository (*NDR*) (https://ndr.ogauthority.co.uk) for the United Kingdom side, and the DISKOS online portal (*Diskos*) (https://portal.diskos.cgg.com) for the Norwegian side.

2D seismic reflection lines:
Diskos: NRS06
NDR: NSR06 (NP062D) (TGS NOPEC)

3D seismic reflection surveys:
Diskos: ST07M06 (ST07M06_mega_south & ST07M06_mega_n) (Equinor ASA)
NDR: MC3D_NNS14 (PGS Exploration UK LTD), which is a merge of:

Survey name (Survey alias)
PP113DGESB (MC3DG11UK_ESB)
PP093DGESB (MC3D_ESB2009)
PP123DGHBR (MC3DG12UK_HBR)
PP103DGESB (MC3D_ESB2010)
PP123DGDUN (MC3D_DUN2012)
PP133DGDUN (MC3D_DUN2013)

Borehole data:
Diskos: NO blocks 31, 32, and 35
NDR: UK quadrants 210, 211, 1, 2, and 3